Investigating cloud absorption effects: Global absorption properties of black carbon, tar balls, and soil dust in clouds and aerosols

Mark Z. Jacobson[1]

Received 23 November 2011; revised 17 January 2012; accepted 24 January 2012; published 21 March 2012.

[1] This study examines modeled properties of black carbon (BC), tar ball (TB), and soil dust (SD) absorption within clouds and aerosols to understand better Cloud Absorption Effects I and II, which are defined as the effects on cloud heating of absorbing inclusions in hydrometeor particles and of absorbing aerosol particles interstitially between hydrometeor particles at their actual relative humidity (RH), respectively. The globally and annually averaged modeled 550 nm aerosol mass absorption coefficient (AMAC) of externally mixed BC was 6.72 (6.3–7.3) m^2/g, within the laboratory range (6.3–8.7 m^2/g). The global AMAC of internally mixed (IM) BC was 16.2 (13.9–18.2) m^2/g, less than the measured maximum at 100% RH (23 m^2/g). The resulting AMAC amplification factor due to internal mixing was 2.41 (2–2.9), with highest values in high RH regions. The global 650 nm hydrometeor mass absorption coefficient (HMAC) due to BC inclusions was 17.7 (10.6–19) m^2/g, ∼9.3% higher than that of the IM-AMAC. The 650 nm HMACs of TBs and SD were half and 1/190th, respectively, that of BC. Modeled aerosol absorption optical depths were consistent with data. In column tests, BC inclusions in low and mid clouds (CAE I) gave column-integrated BC heating rates ∼200% and 235%, respectively, those of interstitial BC at the actual cloud RH (CAE II), which itself gave heating rates ∼120% and ∼130%, respectively, those of interstitial BC at the clear-sky RH. Globally, cloud optical depth increased then decreased with increasing aerosol optical depth, consistent with boomerang curves from satellite studies. Thus, CAEs, which are largely ignored, heat clouds significantly.

Citation: Jacobson, M. Z. (2012), Investigating cloud absorption effects: Global absorption properties of black carbon, tar balls, and soil dust in clouds and aerosols, *J. Geophys. Res.*, *117*, D06205, doi:10.1029/2011JD017218.

1. Introduction

[2] Absorbing aerosol particles affect clouds in several ways: through indirect effects, the rainout effect, the semidirect effect, and cloud absorption effects. The purpose of this study is to elucidate better the global modeled properties of absorbing aerosol components in clouds and the clear sky in order to understand better the cloud absorption effects.

[3] Indirect effects are the increase in cloud reflectivity (first indirect effect) and the decrease in precipitation thus increase in cloud liquid water content and lifetime (second indirect effects) due to the addition of anthropogenic aerosol particles to an evolving cloud [*Gunn and Phillips*, 1957; *Warner*, 1968; *Twomey*, 1972]. Enhanced cloud scattering due to the first indirect effect increases absorption of solar radiation by absorbing aerosols, water vapor, and CO_2 in and around the cloud [*Jacobson*, 2002a]. The reduction in precipitation due to the second indirect effect and the increase in atmospheric stability due to aerosol absorption and scattering also reduce wet removal of aerosols, increasing absorbing aerosol warming by the rainout effect [*Jacobson*, 2002a; *Andreae et al.*, 2004; *Ramanathan and Ramana*, 2005].

[4] The semidirect effect is the change in cloudiness due to the decrease in near-cloud relative humidity (RH) and increase in atmospheric stability caused by absorbing aerosol particles below, within, or above a cloud [*Hansen et al.*, 1997; *Ackerman et al.*, 2000; *Jacobson*, 2002a]. *Hansen et al.*'s original definition was limited specifically to "absorbing aerosols" and considered the effect of constant properties of absorbing aerosols within and outside of clouds on a global scale. All subsequent model treatments of the semidirect effect have similarly assumed that BC and other absorbing aerosols are either externally mixed or internally mixed with the same coating (e.g., at the same RH) outside the cloud as inside the cloud, even in large-eddy simulations where RH varies spatially within a cloud. For example, *Ackerman et al.* [2000] assumed a coated soot core with the same coating within and outside of the cloud. *Johnson* [2005] likewise assumed a uniform mixing ratio of soot and ammonium sulfate throughout the lowest four levels of their model, not accounting for differences in aerosol water content as a function of RH within versus outside the cloud.

[1]Department of Civil and Environmental Engineering, Stanford University, Stanford, California, USA.

0148-0227/12/2011JD017218

[5] Such an assumption, however, does not hold, as aerosol particles interstitially between hydrometeor particles are at the RH of the cloud and swell, thus absorb more strongly by optical focusing, than do aerosol particles within a cloud under the assumption that they are not affected by the cloud RH. In fact, the transition between the ambient RH and the in-cloud RH that aerosol particles are affected by occurs within 0.5 km of a cloud [e.g., *Flores et al.*, 2012].

[6] In addition, scattering by hydrometeor particles enhances the exposure of interstitial absorbing aerosol particles to solar radiation, increasing absorbing aerosol heating more in a cloud compared with the clear sky. Enhanced scattering by clouds is accounted for in any model that solves spectral radiative transfer through a cloud accounting for hydrometeor particle scattering. However, the enhanced scattering increases absorption when swelling versus no swelling by interstitial absorbing aerosols is accounted for.

[7] Like swollen aerosol particles, hydrometeor particles containing absorbing aerosol inclusions absorb more sunlight than do inclusions without a coating. Several studies have examined the potential effects of absorbing aerosol inclusions in hydrometeor particles. *Danielson et al.* [1969] calculated that such inclusions may explain partly why data indicate that thick clouds often have a low albedo. Absorption by inclusions in individual cloud drops has also been included in calculations of drop heating as a function of BC position in the drop [*Chýlek et al.*, 1996]. *Conant et al.* [2002] examined the effects of BC absorption of solar radiation in activating aerosol particles on the critical supersaturation, finding that such absorption reduces the number of particles available for activation at low supersaturation. *Chuang et al.* [2002], *Sandu et al.* [2005], *Erlick et al.* [2006], and *Zhuang et al.* [2010] simulated the 3-D radiative forcing from scenarios with liquid, but not ice, cloud optical properties parameterized as a function of BC volume fraction or single-scattering albedo of the clouds. However, they did not treat the enhanced absorption due to BC interstitially between hydrometeor particles at the RH of the cloud or the physical evolution of BC into hydrometeor particles as a function of size.

[8] *Jacobson* [2006, 2010] accounting for absorption by size-resolved liquid, ice, and graupel hydrometeor particles containing BC inclusions in a global climate model. These studies also treated heating due to size- and composition-resolved aerosol particles containing BC interstitially between the hydrometeor particles, but at the ambient RH. BC entered hydrometeor particles of different size physically in two ways: nucleation scavenging and aerosol-hydrometeor coagulation. The simulations accounted for multiple scattering between hydrometeor particles and within individual hydrometeor particles.

[9] This study tries to elucidate better the characteristics and modeled optical properties of absorbing material within and outside of clouds on a global scale. As part of this effort, it examines the effects on cloud heating of absorption by aerosol inclusions within hydrometeor particles and of absorbing aerosol particles interstitially between hydrometeor particles at the in-cloud RH (as opposed to with clear-sky or constant properties). These two effects are defined here as cloud absorption effects (CAEs) I and II, respectively. They are not considered as part of the semidirect effect, since the semidirect effect has a specific historic definition and application that does not include CAE I or II, and it is important to differentiate different effects of aerosol particles on clouds.

[10] The absorbing aerosol materials quantified here include not only BC, but also certain organic matter and soil dust (SD). All organic aerosol particle constituents absorb short UV wavelengths, but only some absorb long-UV wavelengths and short-visible (blue and some green) wavelengths. The strongest long-UV- and short-visible-wavelength absorbing organics include certain nitrated aromatics, polycyclic aromatic hydrocarbons (PAHs), benzaldehydes, benzoic acids, aromatic polycarboxylic acids, and phenols [*Jacobson*, 1999; *Zhang et al.*, 2011; *Chen et al.*, 2011]. Some of these compounds may be present in tar balls (TB), which are amorphous, spherical aerosol particles 30–500 nm in diameter that form downwind of biomass- or biofuel-burning emissions and that absorb UV and short-visible light wavelengths [*Pósfai et al.*, 2004]. Tar balls comprise about 15 percent of biomass burning particles by number 1.6 km from a fire. Although individually, they are weaker absorbers than BC particles, their size, relative abundance, and strong absorption may cause them to heat biomass burning plumes only slightly less, in aggregate, than do BC emissions in the plumes [*Adachi and Buseck*, 2011]. Tar balls have been found to contain more nitrogen than other types of organic-containing particles [*Adachi and Buseck*, 2011]. Since the addition of nitrogen to an organic compound extends the compound's absorption to longer wavelength, some of the strong UV and short-visible wavelength absorptivity due to tar balls may be due to the presence of nitrogen. Together, all visible-absorbing organics appear brown or yellow and are referred to as brown carbon (BrC).

[11] Another aerosol particle component that absorbs solar radiation is soil dust. Soil-dust particles contain different proportions of Fe_2O_3, Al_2O_3, SiO_2, $CaCO_3$, $MgCO_3$(s), clays, and other substances. Such particles often appear brown or red because they contain iron as hematite [Fe_2O_3]. Iron is also found in industrial particles. Hematite strongly absorbs blue, moderately absorbs green, and weakly absorbs red wavelengths. Because it reflects red and some green, it appears red or reddish-brown in high concentrations. Because of hematite primarily, soil-dust particle absorption increases from the visible to the UV spectra [e.g., *Gillette et al.* 1993; *Sokolik et al.*, 1993]. Soil dust particles also contain aluminum oxide [alumina-Al_2O_3(s)], which absorbs moderately to weakly across the whole visible spectrum and appears silvery white in pure form [*Jacobson*, 2001a]. Aluminum oxide is also found in combustion particles.

[12] Due to the potential importance of BC, BrC, and soil dust in warming the atmosphere, the focus of this paper is on these constituents. The BrC that will be quantified is tar balls although the model also treats the absorption properties of other UV- and short-visible absorbing organics.

2. Description of the Model

[13] The model used for this study was GATOR-GCMOM, a one-way-nested Gas, Aerosol, Transport, Radiation, General Circulation, Mesoscale, and Ocean Model that simulates climate, weather, and air pollution from the global to local scale [*Jacobson*, 2001b, 2010; *Jacobson and Streets*, 2009; *Jacobson et al.*, 2011]. The model simulates feedbacks

Table 1. Aerosol and Hydrometeor Discrete Size Distributions Treated in the Model and the Parameters Present in Each Size Bin of Each Size Distribution[a]

	Aerosol Emitted Fossil-Fuel Soot (EFFS)	Aerosol Emitted Biofuel and Biomass Burning Soot (BFBB)	Aerosol Ultimate Internally Mixed (UIM)	Cloud / Precipitation Liquid	Cloud / Precipitation Ice	Cloud / Precipitation Graupel
Number	Y	Y	Y	Y	Y	Y
BC	Y	Y	Y	Y	Y	Y
POM	Y	Y	Y	Y	Y	Y
SOM	Y	Y	Y	Y	Y	Y
H_2O(aq)-h	Y	Y	Y	Y	Y	Y
H_2SO_4(aq)	Y	Y	Y	Y	Y	Y
HSO_4^-	Y	Y	Y	Y	Y	Y
SO_4^{2-}	Y	Y	Y	Y	Y	Y
NO_3^-	Y	Y	Y	Y	Y	Y
Cl^-	Y	Y	Y	Y	Y	Y
H^+	Y	Y	Y	Y	Y	Y
NH_4^+	Y	Y	Y	Y	Y	Y
Na^+(K, Mg, Ca)		Y	Y	Y	Y	Y
NH_4NO_3(s)		Y	Y	Y	Y	Y
$(NH4)_2SO_4$(s)		Y	Y	Y	Y	Y
Tar balls		Y	Y	Y	Y	Y
Soil dust			Y	Y	Y	Y
Poll/spores/bact			Y	Y	Y	Y
NaCl(s)			Y	Y	Y	Y
H_2O(aq)-c				Y	N	N
H_2O(s)					Y	Y

[a]Y denotes yes. The parameters are the number concentration and chemical mole concentrations. The aerosol distributions contained 14 size bins each (2–50,000 nm diameter), and the hydrometeor distributions contained 30 size bins each (50 nm-12 mm diameter). The components within each size bin of each size distribution were internally mixed in the bin but externally mixed from other bins and other distributions. POM is primary organic matter; SOM is secondary organic matter. S(VI) = H_2SO_4(aq) + HSO_4^- + SO_4^{2-}. H_2O(aq)-h is liquid water hydrated to dissolved ions and undissociated molecules in solution. H_2O(aq)-c is water that condensed to form liquid hydrometeors. Condensed and hydrated water existed in the same particles so that, if condensed water evaporated, the core material, including its hydrated water, remained. H_2O(s) is water that froze or deposited from the gas phase as ice. The emitted species in the EFFS distribution included BC, POM, H_2SO_4(aq), HSO_4^-, and SO_4^{2-}. The remaining species formed by gas-to-particle conversion or crystallization. Sea spray, soil dust, volcanic particle components, pollen, spores, and bacteria were emitted into the UIM distribution. Emitted species in sea spray included H_2O, Na^+, K^+, Mg^{2+}, Ca^{2+}, Cl^-, NO_3^-, H_2SO_4(aq), HSO_4^-, and SO_4^{2-}. Those in biofuel and biomass burning (the BFBB distribution) included the same plus BC, tar balls, and other POM. In both cases, K^+, Mg^{2+}, and Ca^{2+} were treated as equivalent Na^+. Soil dust was generic. Homogenously nucleated aerosol components (H_2O, H_2SO_4(aq), HSO_4^-, SO_4^{2-}, and NH_4^+) entered the UIM distribution. Condensing gases on all aerosol distributions included H_2SO_4 and SOM. Dissolving gases in all aerosol distributions included HNO_3, HCl, SO_2, and NH_3. The hydrated liquid water and H^+ in each bin were determined as a function of the relative humidity and ion composition from equilibrium calculations. All aerosol and hydrometeor distributions were affected by self-coagulation loss to larger sizes and heterocoagulation loss to other aerosol and hydrometeor distributions (except the graupel distribution, which had no heterocoagulation loss).

among meteorology, gases, aerosols, hydrometeors, surfaces, and radiation. Results from it have been compared with gas, aerosol, meteorological, cloud, and optical data in several studies, including those listed above. Some additional comparisons are shown herein.

[14] Meteorological, transport, diffusion, ocean, and other subgrid surface processes were described most recently in the work of *Jacobson and Ten Hoeve* [2012]. Gas processes included emissions, photochemistry, gas-particle conversion, gas-cloud conversion and exchange, gas-precipitation exchange, gas-ocean exchange, advection, convection, molecular diffusion, turbulent diffusion, and dry deposition. Gas photochemistry was solved with SMVGEAR II [*Jacobson*, 1998] among 177 species, 367 kinetic reactions, 7 heterogeneous reactions, and 67 photolysis reactions in the troposphere and stratosphere.

2.1. Aerosol Processes

[15] Aerosol processes were size and composition resolved and included anthropogenic and natural emissions; homomolecular, binary, and ternary homogeneous nucleation; condensation; dissolution; internal-particle chemical equilibrium; aerosol hydration of liquid water as a function of RH, temperature, and composition; ion crystallization within aerosol particles; aerosol-aerosol coagulation; aerosol-hydrometeor coagulation; sedimentation; dry deposition; and transport [*Jacobson*, 2002b, 2003a; *Jacobson et al.*, 2007, 2011]. The model treated three discrete aerosol size distributions, each with 14 size bins and multiple chemicals per size bin (Table 1). Particle number and chemical mole concentrations were tracked in each grid cell over time.

2.2. Convective Cloud, Stratiform Cloud, Aerosol-Cloud Processes

[16] The model simulated cloud thermodynamics and microphysics. For the global domain that was treated here, the model solved for cumulus clouds as subgrid phenomena, allowing for multiple clouds, each with a different base and top height, to form, in each grid column. Stratus were treated at the grid scale, but with a prognostic cloud fraction dependent on stability and moisture gradients. Cloud thermodynamics was constrained by the quasi-equilibrium assumption. Cloud and precipitation microphysics, though, was solved explicitly with time dependence and size and composition resolution [*Jacobson*, 2003a; *Jacobson et al.*, 2007].

[17] During cumulus convection, all aerosol particles and gases were transported vertically within clouds.

Subsequently, water vapor condensed or deposited on the aerosol particles to form hydrometeor particles. The condensation/evaporation and deposition/sublimation equations were solved simultaneously over all aerosol size bins of all three aerosol size distributions and simultaneously for size-resolved liquid, ice, or both. The numerical growth scheme was unconditionally stable and mass conservative. The saturation ratios at equilibrium over each aerosol size bin, used were calculated from Köhler theory assuming the Kelvin effect and Raoult's law affected the equilibrium saturation ratio over liquid water whereas only the Kelvin effect affected that over ice [*Jacobson*, 2003a, 2010].

[18] After (1) growth, the following cloud microphysical calculations were performed: (2) coagulation among liquid ice, and graupel and their aerosol components accounting for diffusiophoresis, thermophoresis, gravitation, Brownian motion, and other coagulation kernels, (3) contact freezing of drops by size-resolved interstitial aerosol particles, (4) heterogeneous plus homogeneous freezing of liquid drops, (5) coagulation of hydrometeor particle and their aerosol inclusions with interstitial aerosol particles, (6) breakup of temporary coalesced liquid drops, (7) sedimentation of liquid, ice, and graupel hydrometeor particles and their aerosol inclusions, (8) coagulation of precipitation hydrometeors with interstitial and below-cloud aerosol particles (washout), (9) removal of precipitation and their aerosol inclusions (rainout), (10) in- and below-cloud evaporation/sublimation to smaller hydrometeor particles and aerosol cores, (11) gas washout, (12) aqueous chemistry within liquid cloud and aerosol particles, (13) heterogeneous chemistry on ice crystals, and (14) lightning production due to size-resolved hydrometeor bounce offs. These processes were all discrete size- and composition-resolved and accounted for the tracking of all aerosol chemical components within all hydrometeor particles of all sizes. Ice crystals formed either by heterogeneous nucleation, contact freezing of liquid drops, homogeneous plus heterogeneous freezing of liquid drops, or evaporative freezing of liquid drops [*Jacobson*, 2003a, 2010].

[19] Aerosol inclusions within hydrometeor particles and aerosol particles interstitially between hydrometeor particles at the RH of the cloud fed back to radiative heating rates and photolysis coefficients in current clouds and the clear sky. In each model column, radiative heating rates were calculated in the clear sky portion once and cloudy sky portion three times each cloud-process time step. The purpose of the first and second calculations through the cloudy sky was to estimate the average temperature change of cloud drops and air during the time step due to absorbing inclusions. The first call was performed with all cloud optical properties. The second, with the same, except with no absorbing inclusions within hydrometeor particles or interstitial absorption. The resulting temperature difference from the beginning to middle of the time step was then used to recalculate evaporation and sublimation rates as a function of hydrometeor size to obtain modified size distributions of hydrometeor particles. Finally, the third radiation call was performed with the modified size distributions to estimate the final heating rates and photolysis coefficients for the time step. These were averaged by cloud fraction with clear-sky values and applied to the grid cells as a whole. Since cloud shrinkage during the time step was determined only for purposes of the radiative calculation, there was no double counting of the heating rates.

[20] In sum, the model treated the first and second indirect aerosol effects, the rainout effect, the semidirect effect, and cloud absorption effect I and II, the major feedbacks of aerosols to clouds.

2.3. Aerosol and Hydrometeor Size Distribution, Composition, and Interactions

[21] Three discrete (multiple size bin) aerosol size distributions and three discrete hydrometeor distributions were treated (Table 1). The three aerosol distributions were an emitted fossil-fuel soot (EFFS) distribution, an emitted combined biofuel-soot and biomass-burning-soot (BFBB) distribution, and an ultimate internally mixed (UIM) distribution, which is the most internally mixed of all distributions. Each distribution contained 14 size bins (2 nm to 50 μm diameter). The three hydrometeor distributions included liquid, ice, and graupel, each with 30 size bins (0.5 μm to 8 mm in diameter). Each size bin of the EFFS distribution contained black carbon (BC), weakly to moderately absorbing primary organic matter (POM), secondary organic matter (SOM), hydrated liquid water, H_2SO_4(aq), HSO_4^-, SO_4^{2-}, NO_3^-, Cl^-, H^+, NH_4^+, NH_4NO_3(s), and $(NH_4)_2SO_4$(s). Each size bin of the BFBB distribution contained these same components plus tar balls, Na^+, K^+, Ca^{2+}, and Mg^{2+}. Each size bin of the UIM distribution contained the same components as the EFFS and BFBB distributions plus soil dust, pollen, spores, and bacteria. Each size bin of each hydrometeor distribution contained the same components as in all three aerosol distribution plus condensed liquid water or deposited ice. Gases, such as HNO_3, HCl, NH_3, H_2SO_4, and organics could condense onto or dissolve into grid-scale EFFS, BFBB, and UIM aerosol particles and dissolve within liquid hydrometeor particles or chemically react on ice and graupel hydrometeor particle surfaces.

[22] At the grid scale, the following discrete size- and composition-resolved aerosol-aerosol coagulation interactions occurred between size distributions: EFFS+EFFS→EFFS; EFFS+BFBB→UIM; EFFS+UIM→UIM; BFBB+BFBB→BFBB; BFBB+UIM— > UIM; UIM+UIM→UIM. Within subgrid clouds, discrete size- and composition-resolved aerosol-hydrometeor coagulation interactions included EFFS+liqUIM→liqUIM, BFBB+liqUIM→liqUIM, UIM+liqUIM→liqUIM, EFFS+iceUIM→iceUIM, BFBB+iceUIM→iceUIM, UIM+iceUIM→iceUIM, EFFS+grauUIM→graupUIM, BFBB+graupUIM→graupUIM, UIM+graupUIM→graupUIM, where liqUIM, iceUIM, and graupUIM are liquid, ice, and graupel distributions and their UIM inclusions, respectively (Table 1). Also within clouds, size- and composition-resolved hydrometeor-hydrometeor coagulation interactions were liqUIM+liqUIM→liqUIM, liqUIM+iceUIM→graupUIM, liqUIM+graupUIM→graupUIM, iceUIM+iceUIM→iceUIM, iceUIM+ graupUIM→graupUIM, graupUIM+graupUIM→graupUIM [*Jacobson*, 2002b, 2003a]. Thus, aerosol particles and their components were tracked within hydrometeor particles, both through cloud formation and precipitation and to snow or sea ice.

[23] When a precipitation particle of a given size fell to snow or sea ice, the aerosol inclusions in that particle were added to the top of the snow or sea ice. The aerosol

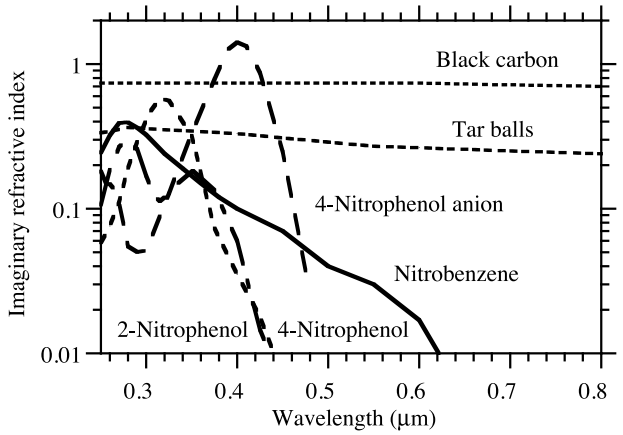

Figure 1. Imaginary refractive indices of BC, nitrated aromatics, and tar balls versus wavelength. BC, nitrated aromatic, and tar ball data were from *Krekov* [1993], *Jacobson* [1999], and *Alexander et al.* [2008], respectively, and references therein.

inclusions slowly migrated through the snow or ice [*Jacobson*, 2004].

[24] The model also treated formation of subgrid aircraft contrails from aerosol particles emitted by aircraft and the subsequent release of aerosol cores in contrail particles to the grid scale, affecting cirrus clouds, as described in the work of *Jacobson et al.* [2011].

[25] Microphysical parameters, such as coagulation coefficients, particle fall speeds, Knudsen numbers, and diffusion coefficients, in the EFFS and BFBB distributions were calculated assuming BC was an aggregate with a fractal dimension of 1.7 [*Jacobson and Seinfeld*, 2004]. In the UIM distribution, BC was assumed to have compacted to a sphere due to greater aging and internal mixing in this distribution.

2.4. Radiative Processes

[26] For radiative transfer calculations, each model column was divided into clear- and cloudy-sky portions, and separate radiative transfer calculations were performed for each. As described in section 2.2, radiative transfer was solved three times through the cloudy portion of each grid column each cloud-process time step. Radiative transfer was solved in each case through multiple layers of air and one layer of snow, sea ice, or ocean water in order to calculate, rather than prescribe, spectral albedos over these surface. Albedos in these cases were calculated as the upward divided by the downward irradiance predicted at the top of each surface layer each time step. Snow, sea ice, and ocean water optical properties were determined as a collection of large spheres of specific size that resulted in spectral albedos that matched data [*Jacobson*, 2004]. Ocean albedos accounted for phytoplankton optical properties. Since the model tracked BC, TB and other BrC, SD, and all other aerosol inclusions within precipitation, which fell onto snow and sea ice, the radiative transfer calculation accounted for the optics of all absorbing aerosol constituents within and between snow and sea ice particles [*Jacobson*, 2004, 2010] as well as within aerosol particles and within and between hydrometeor particles. Thus, the model treated the microphysical and radiative effects of aerosols on clouds, precipitation, snow, and sea ice.

[27] The radiative transfer code of *Toon et al.* [1989] was used to solve for atmospheric heating rates and actinic fluxes over each of 694 wavelengths/probability intervals with gas absorption coefficients from *Jacobson* [2005]. Aerosol and cloud optical properties were calculated by integrating spectral optical properties over each size bin of each aerosol and hydrometeor particle size distributions. In all aerosol particle size distributions, BC was treated as a spherical core surrounded by a mixed shell for optical calculations [*Ackerman and Toon*, 1981]. Prior to each radiative transfer calculation, the liquid water content (LWC) of aerosol particles interstitially between hydrometeor particles was calculated at the RH of the cloud with the EQUISOLV II chemical equilibrium code [*Jacobson*, 2002b]. Outside of clouds, the LWC was determined at the ambient RH with EQUISOLV II. Optical properties of nonspherical ice crystals and graupel were determined with a Mie code [*Ackerman and Toon*, 1981] assuming these particles were a collection of spheres that had the same total volume to area ratio and total volume as the nonspherical particles [*Grenfell and Warren*, 1999].

[28] Historically, the model has treated UV, visible, and/or solar-IR absorption by BC; non-tar-ball BrC, and soil dust and thermal-IR absorption by all aerosol particle constituents [*Jacobson*, 1999, 2001a]. Here, optical properties of tar balls are also considered. Refractive index data for BC were from *Krekov* [1993] and references therein; data for weakly, moderately, and strongly absorbing non-tar-ball organic and weakly absorbing organics were from *Jacobson* [1999] and *Kirchstetter et al.* [2004]; data for tar balls were from *Alexander et al.* [2008]; and for soil dust were from *Fukushima et al.* [2003]. Figure 1 shows the spectral refractive indices of some of these constituents.

[29] For BC, the refractive index at 550 nm was $1.833–0.74i$ and the density assumed was 1.5 g/cm^3. The refractive index is close to that of the void fraction line in the work of *Bond and Bergstrom* [2006, Figure 7], which is a straight line denoting ideal ratios of imaginary to real refractive indices. The density is justified as follows: *Jacobson* [2000] used a baseline density of 1.25 g/cm^3 derived by scaling the density of crystalline graphite at 550 nm of 2.25 g/cm^3 by the ratio of the imaginary refractive index used there (0.74) to that of graphite, (1.34). That density appears physical for the imaginary refractive index used. Here, however, the density was increased to 1.5 g/cm^3 as a compromise between the 1.25 g/cm^3 and 1.8 g/cm^3, used by *Bond and Bergstrom* [2006], which accounts for greater compaction of soot aggregates as they age. Coincidentally, *Kahnert* [2010] pointed out that BC densities of 1.3–1.7 g/cm^3 are needed (and 1.8 g/cm^3 is too high) to explain observed MACs of externally mixed BC when refractive indices along the void fraction line are assumed, and indeed, a density of 1.5 g/cm^3 does result in good agreement of mean modeled with measured MACs, as discussed shortly.

[30] Since all aerosol component concentrations were tracked within each size of each hydrometeor particle type (liquid, ice, and graupel) throughout the evolution of clouds and precipitation, it was possible to calculate cloud absorption due to BC, BrC (including TB), and SD inclusions in clouds. Aerosol material could enter hydrometeor particles

by either nucleation scavenging or aerosol-hydrometeor coagulation. During nucleation scavenging, each hydrometeor particle of a given size formed on top of a multicomponent aerosol particle of a single size. During aerosol-hydrometeor coagulation, aerosol particles of different size coalesced with hydrometeor particles of each size, so each hydrometeor particle of each size now contained aerosol inclusions of multiple sizes. The total mass of each aerosol component summed over all aerosol sizes entering each size hydrometeor particle was tracked, but the size distribution of the aerosol component within each hydrometeor particle was not tracked, although it could be with the use of a lot more memory and computer time.

[31] Three practical ways to treat absorption by aerosol inclusions in hydrometeor particles are (1) as a single large absorbing core surrounded by a water shell, (2) a uniform mixture of absorbing material and water, and (3) aerosol inclusions randomly dispersed throughout the hydrometeor particle. Whereas a single core surrounded by a shell may be physical for aerosol particles, particularly aged ones where the amorphous core has compacted to a spherical shape, it is less physical for a hydrometeor particle, which may have multiple inclusions due to aerosol-hydrometeor coagulation. However, as a hydrometeor particle shrinks, the inclusions compress to a single core, so the core-shell approximation is more physical for the latest stage of cloud decay. The well-mixed approximation is unphysical because BC, for example, is not dissolved in solution so cannot physically mix uniformly throughout a drop.

[32] The most physical method of treating absorbing inclusions is to assume they are randomly dispersed throughout a hydrometeor particle. This method is applied here with the iterative dynamic effective medium approximation (DEMA) [*Chýlek et al.*, 1984], as described by *Jacobson* [2006]. With this method, one or multiple absorbing spherical inclusions are located randomly throughout each hydrometeor particle, and effective refractive indices are determined for the hydrometeor particle as a whole as a function of wavelength. As stated, the mass (thus volume) of each aerosol component size was tracked inside each hydrometeor particle. Because the aerosol inclusion size distribution for each component was not tracked in each hydrometeor particle, it was necessary to assume a size-distribution of the known mass within each hydrometeor particle of a given size to use with the DEMA.

[33] The simplest method is to assume inclusions are of uniform size and calculate the number of inclusions from the total volume of each chemical inclusion in each hydrometeor size (which is known) divided by the volume of a single inclusion (assumed). This was done for BC in the work of *Jacobson* [2006]. However, if the total volume of a chemical inclusion is less than the assumed volume of a single inclusion, this results in a fractional inclusion. Here, it is assumed that if the total volume of a chemical inclusion is less than that of a single inclusion, one inclusion at its exact size, randomly located in the drop, is assumed; otherwise, the number of inclusions is calculated as before. This assumption makes more physical sense. It implies that, for small total inclusion volume in a hydrometeor particle, the particle likely contains one inclusion; otherwise, it contains multiple inclusions. Assuming one inclusion of an exact size results in a slightly different answer with the DEMA than assuming a fractional inclusion of a larger size because the inclusion diameter differs.

[34] For BC, the transition diameter between one and multiple inclusions was selected as 200 nm. The effect of this assumption on the heating rate is examined in sensitivity tests here. For tar balls, the same transition diameter was assumed as for BC. For soil dust, the transition diameter was assumed to be 3 μm. An advantage of the DEMA is that it is valid for larger size parameters ($x = \pi d/\lambda$, where d is inclusion diameter and λ is wavelength) than other effective medium approximations [*Chýlek et al.*, 1984]. However, x in general is ideally not much larger than unity. Further, in the present application, it is necessary to calculate the effects of SD, TB, and BC inclusions of different size simultaneously in the same particle hydrometeor particle. This was done by converting the total volumes of SD and TB to an effective volume of BC, adding those effective volumes to the actual volume of BC, then determining the number of resulting inclusions. In other words, the volumes of SD and TB particles were reduced to the volume of BC particles that give the same absorption as the correct volume of SD and TB. The effective volume of SD converted to BC was calculated as the actual volume of SD multiplied by the ratio of the single-particle absorption optical depth of SD at its actual size (as an externally mixed aerosol particle) to that of BC at its actual size. A similar equation was used for TB. The resulting heating of a given hydrometeor particle attributable to each BC, SD, and TB was assumed to be proportional to the equivalent BC volume of each component.

2.5. Emissions

[35] Table 2 provides the global speciated particle emissions from fossil fuels, biofuels, and biomass burning as well as the gas-phase emissions from several sources for this study. The baseline emissions from land-based anthropogenic sources and shipping were derived substantially from the 0.5° resolution IPCC AR5 2005 inventory (Intergovernmental Panel on Climate Change, IPCC ARG historic emission and scenario data for chemistry simulations, online, ftp://ftp-ipcc.fz-juelich.de/pub/emissions/, 2009). The baseline flight-by-flight aircraft emission inventory used (over 30 million flights worldwide) was the 2006 inventory described in the work of *Wilkerson et al.* [2010]. For biomass burning, fine-particle BC and POC emission rates were obtained by combining satellite-derived 8 day fuel burn data [*Giglio et al.*, 2006] with land use data (to determine fire type) and emission factors [*Andreae and Merlet*, 2001]. Fuel burn data were available for 5 separate years. For biofuel burning, the spatial distribution of BC and POC emissions from *Bond et al.* [2004] were used, but the global fuel burn rate was adjusted with uncertainty ranges from *Ludwig et al.* [2003].

[36] For biomass and biofuel burning, emission rates of particle components K^+, Na^+, Ca^{2+}, Mg^{2+}, NH_4^+, Cl^-, SO_4^{2-}, and NO_3^-, and gases H_2, H_2O, NO, NO_2, N_2O, NH_3, SO_2, CO, CO_2, CH_4, CH_3OH, CH_3Cl, CH_3Br, C_2H_4, C_2H_6, C_3H_6, C_3H_8, HCHO, HCOOH, CH_3COOH, CH_3CHO, CH_3COCH_3, C_4H_6, C_5H_8, C_6H_6, C_6H_5CHO, $C_6H_5CH_3$, $C_6H_4CH_3CH_3$, and CH_3SCH_3 were obtained by multiplying BC biomass emission rates by the ratio of a mean biofuel or biomass emission factor [*Andreae and Merlet*, 2001; *Ferek et al.*, 1998] for each component to that of BC. Tar ball emission

Table 2. World Fine-Particle Global Emission Rates of Black Carbon, Primary Organic Carbon, and Other Particle Components in Soot From Fossil Fuels, Solid Biofuels, and Open Biomass Burning[a]

	Aircraft	Shipping	All Other Fossil Fuel	Total Fossil Fuel (Aircraft Plus Shipping Plus All Other Fossil Fuel)	Biofuel	Biomass Burning	Total (Total Fossil Fuel Plus Biofuel Plus Biomass Burning)
BC	0.0072	0.144	3.14	3.29	3.33	2.70	9.32
POC	0.0072	0.153	4.48	4.64	8.97	12.5	26.1
Tar balls	–				3.85	5.33	9.18
S(VI)	0.00094	0.0014	0.054	0.056	0.55	0.74	1.35
Na^+	–	–	–	–	0.030	0.026	0.056
K^+ as Na^+	–	–	–	–	0.21	1.57	1.78
Ca^{2+} as Na^+	–	–	–	–	0.21	0.29	0.50
Mg^{2+} as Na^+	–	–	–	–	0.092	0.17	0.26
NH_4^+	–	–	–	–	0.006	0.029	0.035
NO_3-	–	–	–	–	0.29	0.25	0.54
Cl^-	–	–	–	–	0.55	0.41	0.96

[a]World fine-particle is <1 μm diameter. Black carbon is BC. Primary organic carbon is POC. Units are Tg-C/yr for BC, POM, and tar balls and Tg-species/yr for all others; S(VI) = $H_2SO_4(aq)+HSO_4^-+SO_4^{2-}$, where the distribution was determined within each size bin (Table 1) with an equilibrium calculation, accounting for hydrated H_2O and H^+, which were also tracked. For biomass burning, emission rates shown are those averaged over 5 years for which burn data were available (2002–2006). In the model, the 5 year cycle was repeated. For biofuel burning, the spatial distribution of BC and POC emissions from *Bond et al.* [2004] were used, but the global fuel burn rate from *Bond et al.* [2004] was increased to 4200 Tg-dry matter (dm) /yr, which in the mean of the uncertainty range of *Ludwig et al.* [2003] of 1086–6192 Tg-dm/yr for 1995 multiplied by the 2009 to 1995 world population. Emission factors for biofuel gases and K^+ were obtained from *Andreae and Merlet* [2001]. Biofuel-burning emission factors for other particle components were approximated as grass emission factors from *Ferek et al.* [1998], as these were closest to the biofuel emission factors of *Andreae and Merlet* [2001] for BC and POC. Coarse-particle fossil-fuel emissions were 0.075 those of fine BC and 0.35 those of fine POC, respectively; coarse biofuel and biomass-burning BC and POC were 0.2 and 0.35 those of fine BC and POC, respectively. The primary organic matter (POM) to POC ratio was 1.6:1 for fossil fuels and 2:1 for biofuel burning and biomass burning. Biofuel burning emissions of 39 biofuel gases and bond groups were as follows: (Tg-gas/yr): CO_2: 8756; H_2O: 2987; CH_4: 21.4; C_2H_6: 4.13; C_3H_8: 1.40; NO: 9.0; NO_2: 1.41; HONO: 0.13; CO: 389; CH_3OH: 3.65; C_2H_5OH: 1.31; HCHO: 0.67; CH_3CHO: 3.79; higher aldehydes: 7.65; CH_3COCH_3: 0.14; C_2H_4: 8.67; C_3H_6: 3.82; C_4H_6: 1.33; HCOOH: 5.42; CH_3COOH: 7.07; benzene: 5.19; toluene: 2.23; benzaldehyde: 0.14; xylene: 1.08; isoprene: 1.55; monoterpenes: 0.85; $HOCH_2CHO$: 3.73; acetol: 54.2; SO_2: 13.3; SO_3: 0.29; H_2SO_4: 0.062; OCS: 0.23; NH_3: 0.53; H_2: 6.99; N_2O: 0.34; CH_3Cl: 0.31; CH_3Br: 0.017. paraffin bond group: 5.09; olefin bond group: 4.16. The CO_2 emissions are biofuel combustion emissions, not combustion minus regrowth emissions, as the model calculated photosynthesis online, accounting for biofuel regrowth. Global emissions of non-biofuel, non-biomass anthropogenic methane were 260 Tg-CH_4/yr, fossil-fuel CO_2 were 26,454 Tg-CO_2/yr, and anthropogenic N_2O were 6.94 Tg-N_2O/yr.

rates from biomass and biofuel burning were assumed to be 30% of total non-TB POC+TB emission rates by mass (or 20% of total POC+BC mass emissions but 0% of fossil fuel emissions. *Adachi and Buseck* [2011] found that 1–14% of all biomass burning particles by number were tar balls, 57–64% were other organic particles, and 16–33% were BC within 4 min of burns. The fact that most tar balls are in the accumulation mode (mean diameter 210+/−100 nm), whereas other organics and BC are generally smaller, justifies a larger mass fraction than number fraction of tar balls.

[37] Natural emissions from lightning (NO, NO_2, HONO, HNO_3, N_2O, H_2O_2, HO_2, CO), soils (dust, bacteria, NO, N_2O, H_2, CH_4, H_2S, DMS, OCS, CS), oceans (bacteria, sea spray, DMS, N_2O, H_2, CH_4, CH_3Cl), and vegetation (pollen, spores, isoprene, monoterpenes, methanol, other VOCs) were calculated as a function of meteorology as in the work of *Jacobson and Streets* [2009].

3. Model Simulations and Results

[38] Global simulations were run at 4°SN × 5°WE horizontal resolution and 68 vertical sigma-pressure layers from the ground to 0.219 hPa (≈60 km), with 15 layers from 0 to 1 km and 500 m resolution from 1 to 21 km. The center of the lowest model layer was 15 m above ground. The model was initialized with 1° × 1° reanalysis meteorological fields (Global forecast system, online, http://nomads.ncdc.noaa.gov/data/gfs-avn-hi/, 2007) for simulations starting 1 January 2006 and run forward in time with no data assimilation. Initial atmospheric burdens of all gases and aerosol particles changed over time. Because this study does not present climate responses, only 2 year simulations were run. Results after 2 years were very similar to results after 1 year, and results for 2006 only are shown to compare with some data for that year. Results for several parameters were also similar to results after 15 years from *Jacobson* [2010], as discussed shortly.

3.1. Emission, Dry Deposition, and Wet Deposition Fluxes

[39] Table 3 shows the annually averaged emission, dry deposition, and wet deposition mass fluxes of BC and SD in the model. Whereas 94.4% of the BC total deposition flux was wet, 75.7% of the SD deposition flux was wet due to

Table 3. Summary of Globally Averaged Annual Emission Fluxes, Dry Deposition Fluxes, and Wet Deposition Fluxes for Black Carbon and Soil Dust Over 1 Year Of Simulation[a]

	Black Carbon	Soil Dust
Emissions flux (kg/m^2/s)	6.36×10^{-13}	1.17×10^{-10}
Wet deposition flux (kg/m^2/s)	6.07×10^{-13}	8.49×10^{-11}
Dry deposition flux (kg/m^2/s)	3.63×10^{-14}	2.73×10^{-11}
Wet+dry flux (kg/m^2/s)	6.44×10^{-13}	1.12×10^{-10}
% of deposition that is wet	94.4	75.7
Time-average aerosol loading (Tg)	0.089	23.3
Lifetime (days)	3.2	4.5

[a]The wet deposition fluxes for black carbon is summed over the EFFS, BFBB, and UIM aerosol size distributions, each with 14 size bins, and the soil dust is summed over the UIM distribution. The difference between the emission flux and wet plus dry deposition flux is the difference between the initial and final atmospheric loadings (the initial loading for BC was ∼0.214 Tg and that of soil dust ∼14.6 Tg). The BC loading dropped close to its final loading within a few days. The modeled area of the Earth was $5.09238842 \times 10^{14}$ m^2.

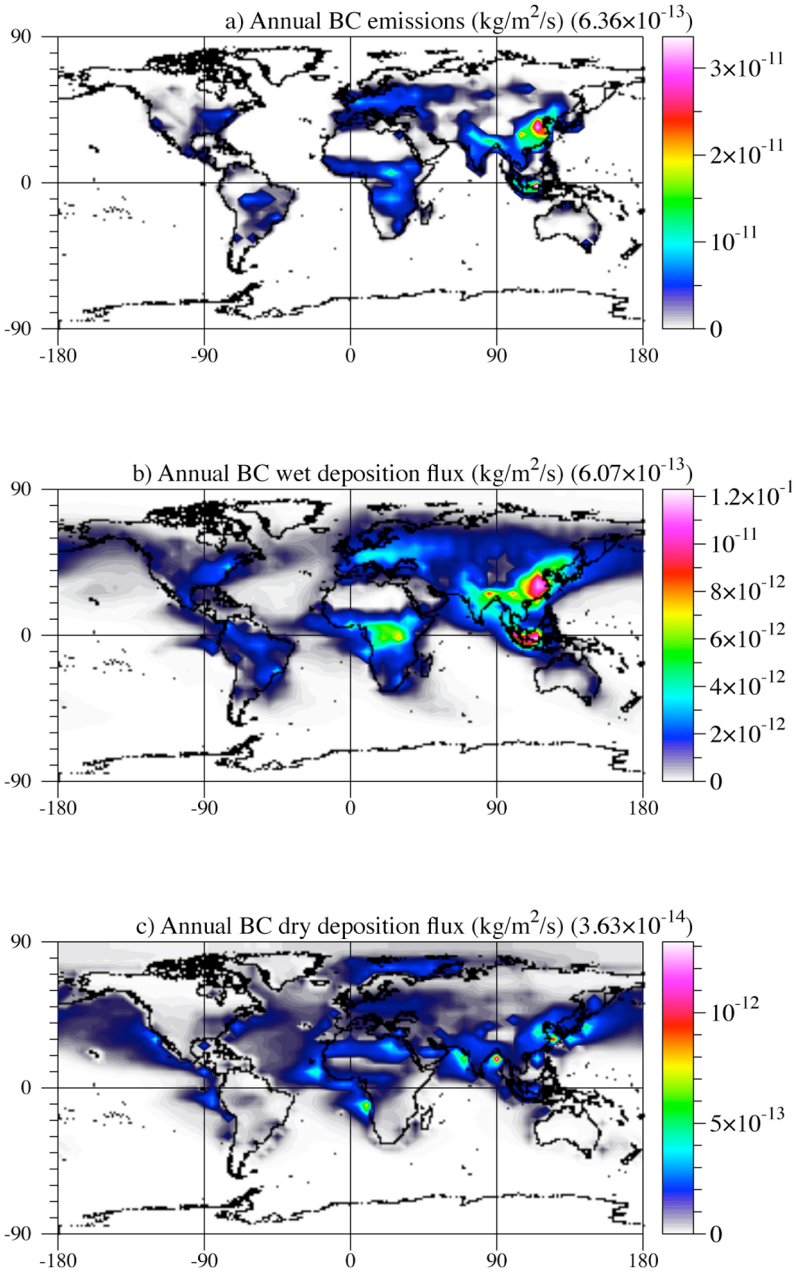

Figure 2. Annually averaged modeled BC (a) emission flux, (b) wet deposition flux, and (c) dry deposition flux.

the fact that SD particles are larger thus fall out more readily away from precipitation than does BC. For comparison, *Jacobson* [2010] similarly calculated that 91.5% of BC deposition flux was wet when the model was run with 47 layers versus 68 layers here. The slight difference is due to the slightly higher rainfall rate compared with that study.

[40] Figures 2–4 show the annually averaged spatial distributions of the modeled BC, TB, and SD all-source emission, wet-deposition, and dry-deposition fluxes. BC emissions sources included fossil-fuel combustion, biofuel combustion, and open biomass burning. Although wet-deposition fluxes were much larger than were dry-deposition fluxes of BC, dry deposition fluxes were spread more evenly over a larger area of the world, particularly the Arctic, since most wet deposition occurred at low and mid latitudes. For example, whereas the ratio of wet to dry deposition at mid latitudes was ~10, that over the Arctic was ~2. Thus, about one third of the BC deposited on Arctic ice was from dry deposition, whereas two thirds was from wet deposition.

[41] The opposite phenomenon occurred for soil dust. In that case, the wet deposition flux was more evenly spread out globally than the dry deposition flux. The reason is the largest soil dust particles were so heavy, they fell out quickly and only the smaller ones remained to be removed by wet

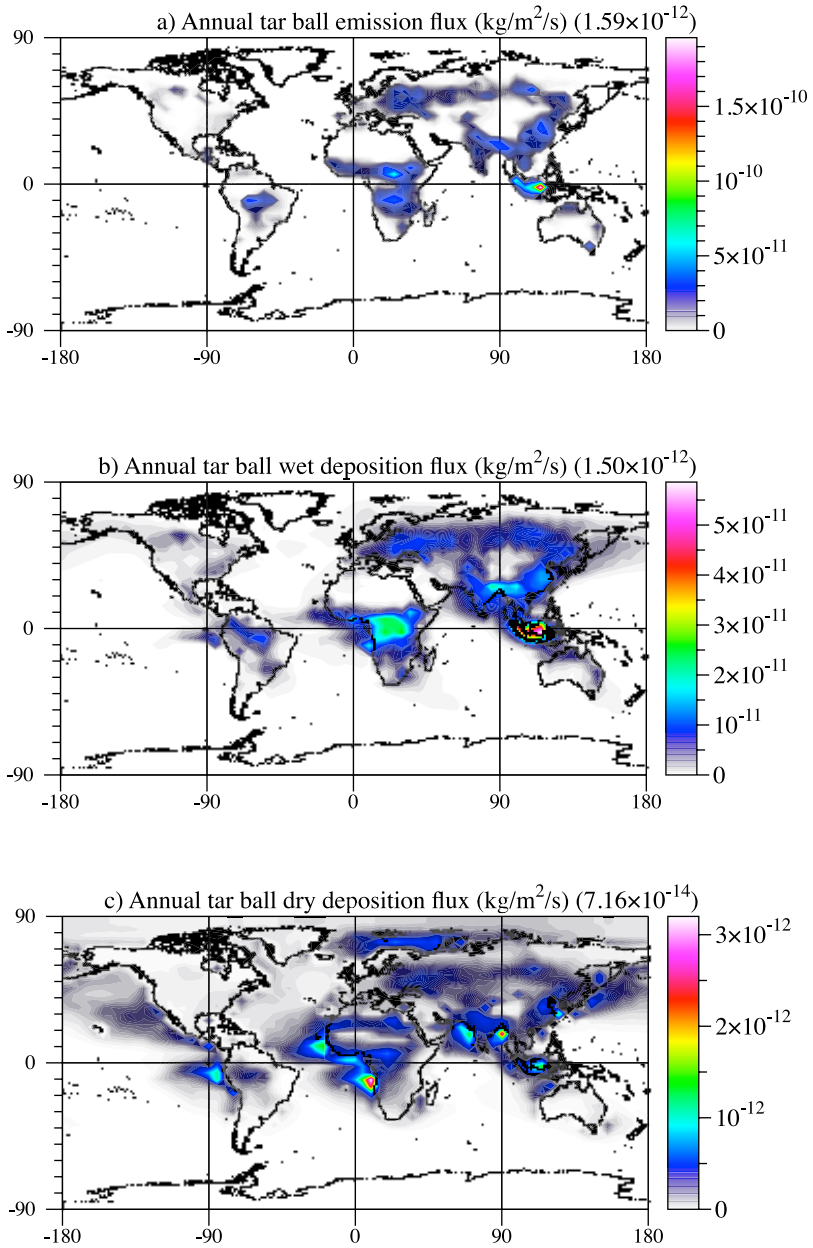

Figure 3. Annually averaged modeled tar ball (a) emission flux, (b) wet deposition flux, and (c) dry deposition flux.

deposition. Nevertheless, about a third of soil dust that made it to the Arctic was dry deposited; the rest was wet deposited.

[42] Of all emitted BC mass in the EFFS distribution, ~95.2% was lost by coagulation to the BFBB and UIM distributions, ~3.36% was lost to hydrometeor particles and then to wet deposition, ~1.45% was lost by dry deposition, and a residual remained in the air. Of all emitted BC mass emitted to the BFBB distribution, ~85.3% was lost by coagulation to the UIM distribution, ~14.4% was lost by wet deposition, and ~0.16% was lost by dry deposition. Of all BC mass coagulated into the UIM distribution, ~94.3% was lost by wet deposition, ~5.6% was lost by dry deposition, and a residual remained in the air.

[43] The modeled internal-mixing time of EFFS BC due to coagulation was ~3 h. That of BFBB BC due to coagulation was ~13 h. The 3 h internal-mixing time for EFFS particles is similar to that of BC found by *Moffet and Prather* [2009] from data in an urban area and from *Jacobson* [2010], who considered only two size distributions rather than three. EFFS particles internally mixed faster than did BFBB particles because the former were emitted mostly in urban areas, closer to more UIM particles than were BFBB particles. Condensation onto the EFFS and BFBB particles occurred simultaneously with coagulation but did not move such particles to the UIM distribution.

3.2. Dry and Wet Deposition to Snow and Sea Ice

[44] The model calculated that, worldwide, only ~0.46% of BC that deposited to any snow or sea ice was dry deposited; the rest was wet deposited. Most of the BC that

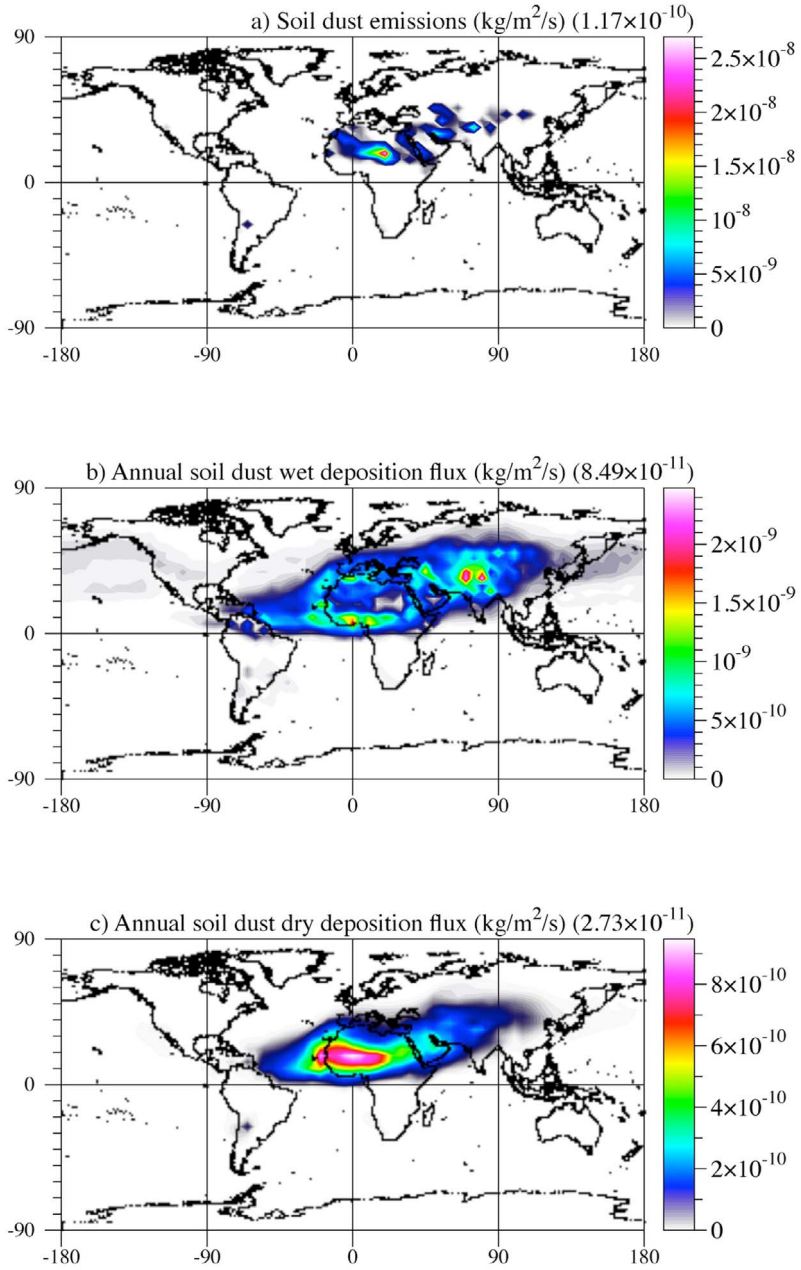

Figure 4. Annually averaged modeled soil dust (a) emission flux, (b) wet deposition flux, and (c) dry deposition flux.

deposited to snow or sea ice deposited to snow over Eastern Europe (Figure 5). On the other hand, about 2.6% of soil dust that deposited to snow or sea ice was dry deposited. Most soil dust that deposited to snow or sea ice deposited to snow over Russia and China and in the Himalayas (Figure 6).

3.3. Column Loadings in the Clear Sky and Clouds

[45] Figures 7a–7c show the annually averaged column loadings of BC in each of the three aerosol size distributions treated, the EFFS, BFBB, and UIM distributions. BC emissions occurred into the EFFS and BFBB distributions, and coagulation moved emitted particles to larger sizes and/or to the UIM distribution. The burdens accounted for aerosol BC in the clear sky and interstitially between hydrometeor particles, but not as inclusions in hydrometeors particles, as these will be shown separately. The highest annually and globally averaged concentration of aerosol BC was in the UIM distribution (Figure 7c). Tar balls were emitted only into the BFBB distribution from both biofuel and biomass-burning emissions sources. Most of the mass of tar balls ended up in the UIM distribution (Figures 7d and 7e). Soil dust was emitted only into the UIM distribution. The bulk of its loading was over the Sahara desert (Figure 7f).

[46] The mean atmospheric loading of total aerosol BC in the model (0.089 Tg = 0.175 mg/m^2) is within the range of loadings from *Forster et al.* [2007] (0.15–0.47 mg/m^2) although slightly lower than the result of *Jacobson* [2010]

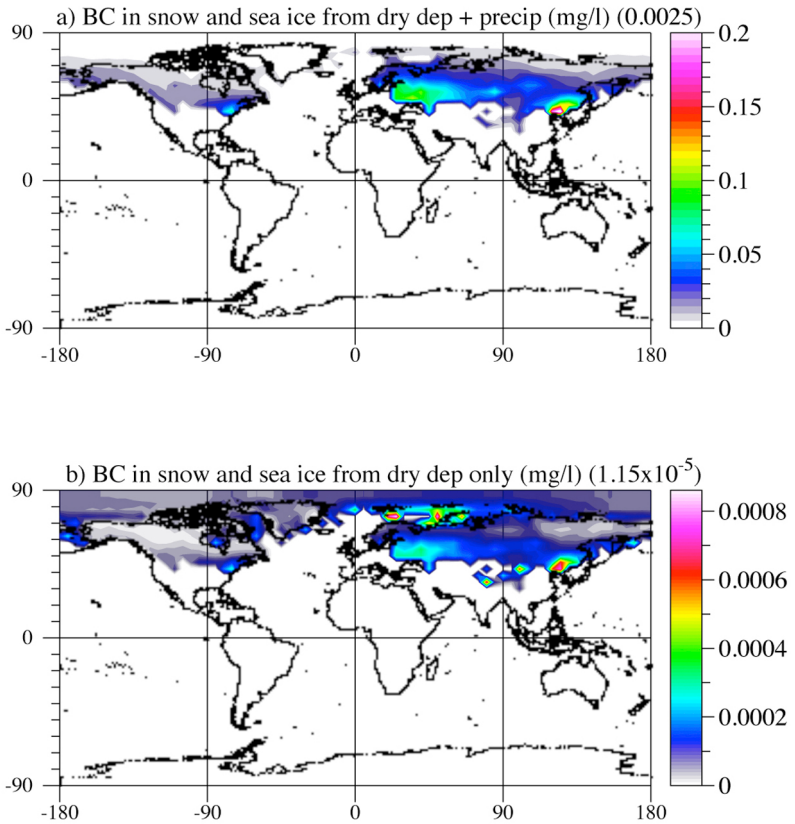

Figure 5. Annually averaged modeled concentration of BC in snow and sea ice from (a) wet plus dry deposition and (b) dry deposition only.

(0.128 Tg = 0.251 mg/m^2) due to the greater wet removal rate here during 1 year. Dividing the mean column loading by the summed wet plus dry deposition fluxes gives overall *e* folding lifetimes of BC and soil dust against removal of 3.2 and 4.5 days, respectively (Table 3). The longer lifetime of soil dust despite its larger dry deposition flux is due to the fact that most of it is emitted in clear-sky locations, so it takes longer to encounter rainfall. These physically based lifetimes, which accounted for discrete size resolution of aerosols containing BC and their interactions with size-resolved clouds and precipitation, compare with assumed or empirically parameterized values of 4.4–11.4 days among 11 empirically based models [*Schulz et al.*, 2006].

[47] Figure 8 shows the annually averaged modeled column loadings of BC, TB, and SD as inclusions in cloud and precipitation particles. The largest in-cloud column burdens in all cases occurred over source regions, except for soil dust, which had a greater burden in hydrometeor particles offshore the Sahara and over the Middle East and Southwestern Asia than over the Sahara itself. The reason is that clouds rarely formed over the Sahara desert itself compared with these other locations, so not much soil dust was incorporated into clouds there. The globally and annually averaged hydrometeor-inclusion loadings of BC, tar balls, and soil dust, were about 2.3%, 3.1%, and 2.8% the respective aerosol loadings. These averages are not in-cloud averages but grid-cell and time-averages, accounting for times with no clouds. Addition BC resided interstitially between hydrometeor particles.

3.4. Monthly Comparisons With Aeronet, OMI, and HIPPO Data

[48] Figure 9a–9j compares monthly modeled total clear-sky aerosol absorption optical depth (AAOD) at 550 nm with AERONET data [*Holben et al.*, 2001] at 10 stations over four continents and the Atlantic Ocean. Modeled aerosol absorption at this wavelength was due to BC, TB, SD, and some non-TB organic material. Given the coarse global model resolution (4° × 5°) and the fact that the comparisons were obtained by using bilinear interpolation among four surrounding model grid cells to each AERONET site, the comparisons are encouraging. Most errors occurred in November and December.

[49] Figure 10a shows a map of 2006 modeled and multiyear-averaged AERONET (dots) clear-sky 550 nm AAOD at all 420 stations that data were available for. Figure 10d shows a scatterplot of all modeled values at the locations of the measurements in Figure 10a. Figure 10b shows a map of 2006 OMI (Ozone Monitoring Instrument on the EOS-Aura satellite) 500 nm AAOD [*Torres et al.*, 2007]. OMI 500 nm AAODs are a Level 2 data product derived at 388 nm and extrapolated with modeling to 500 nm. Nonzero data were averaged daily to obtain monthly values if at least seven daily values were available. Nonzero monthly values were averaged to obtain annual values for pixels with at least four months of nonzero data (D. Whitt, personal communication, 2011). Figures 10e and 10f show correlations between AERONET and OMI at all AERONET sites

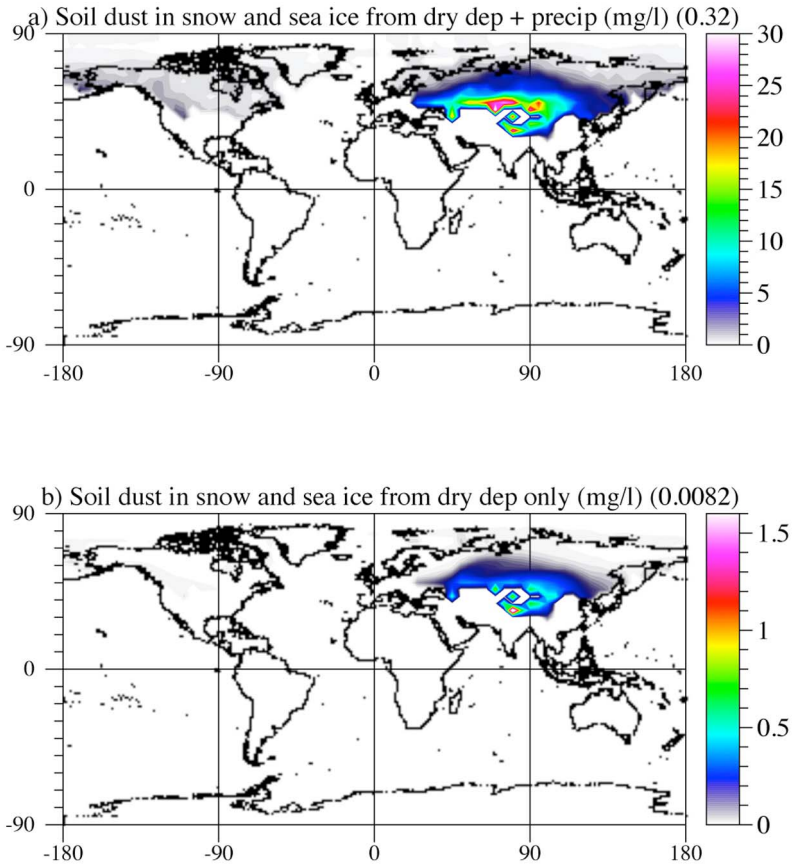

Figure 6. Annually averaged modeled concentration of soil dust in snow and sea ice from (a) wet plus dry deposition and (b) dry deposition only.

where OMI values were nonzero and between OMI and the model for the same AERONET sites, respectively.

[50] The correlation plots indicate that the model correlated slightly better independently with AERONET ($r = 0.46$, $p < 0.0001$) and with OMI ($r = 0.41$, $p < 0.0001$) than AERONET correlated with OMI ($r = 0.40$, $p < 0.0001$) when comparisons were limited to AERONET sites. Further, the model average 550 nm AAOD at all AERONET sites (0.023) was slightly larger than the AERONET values at those sites (0.019), but slightly lower than OMI AAODs (0.024) at those AERONET sites where OMI data were available. The model average over all land was only 11% greater than OMI average over land, although the OMI data did not include all land or most of the ocean. The relative consistency of the model compared with data contrasts with some earlier studies that found model underpredictions of AAOD with AERONET data in particular [*Sato et al.*, 2003; *Reddy et al.*, 2005], most likely due to the treatment of BC as externally mixed as opposed to evolving between external and internal mixing.

[51] Figures 10d and 10e indicate that both the model and OMI data underpredicted the maximum measured AAODs but overpredicted the minimum values compared with AERONET. As a result, the correlation between OMI and the model (Figure 10f) shows less extreme variation.

[52] Some uncertainties in AERONET data arise due to the fact that measurements were made only during the day, and not all months of data were available at all 420 locations, so averages were taken over only available months. Similarly, OMI data were available for different days at different locations and gathered only during overpass times and primarily when clouds were absent or at low cloud optical depth. Modeled values were obtained day and night in all clear-sky portions of a grid column. Major model uncertainties include the prediction of the right amount of soil dust spatially and temporally and the optical properties and quantity of tarballs as well as the BC emission inventory over southeast Asia. Despite these uncertainties, the close proximity of the averages and the correlations between the model and each data set compared with that between the data sets suggests that the model is unlikely to be overpredicting global mean aerosol absorption optical depth.

[53] Figure 10c shows the 650 nm cloud absorption optical depth (CAOD) resulting from inclusions only (not aerosol particles interstitially between hydrometeor particles, which would be accounted for in the cloudy-sky AAOD. The CAOD accounted primarily for the absorption due to BC, TB, and SD Globally and time-averaged (thus accounting for times and locations with and without clouds), the 650 nm CAOD (0.00066) was about 8.5% that of the clear-sky aerosol absorption optical depth (AAOD) at 650 nm (0.0078). For comparison, the clear-sky 550 nm AAOD was 0.014 (Figure 10a), the all-sky 550 nm AAOD was 0.011, and the clear-sky 550 nm AOD was 0.0158. The all-sky AAOD was lower than the clear-sky value because some aerosol particles in clouds became inclusions in

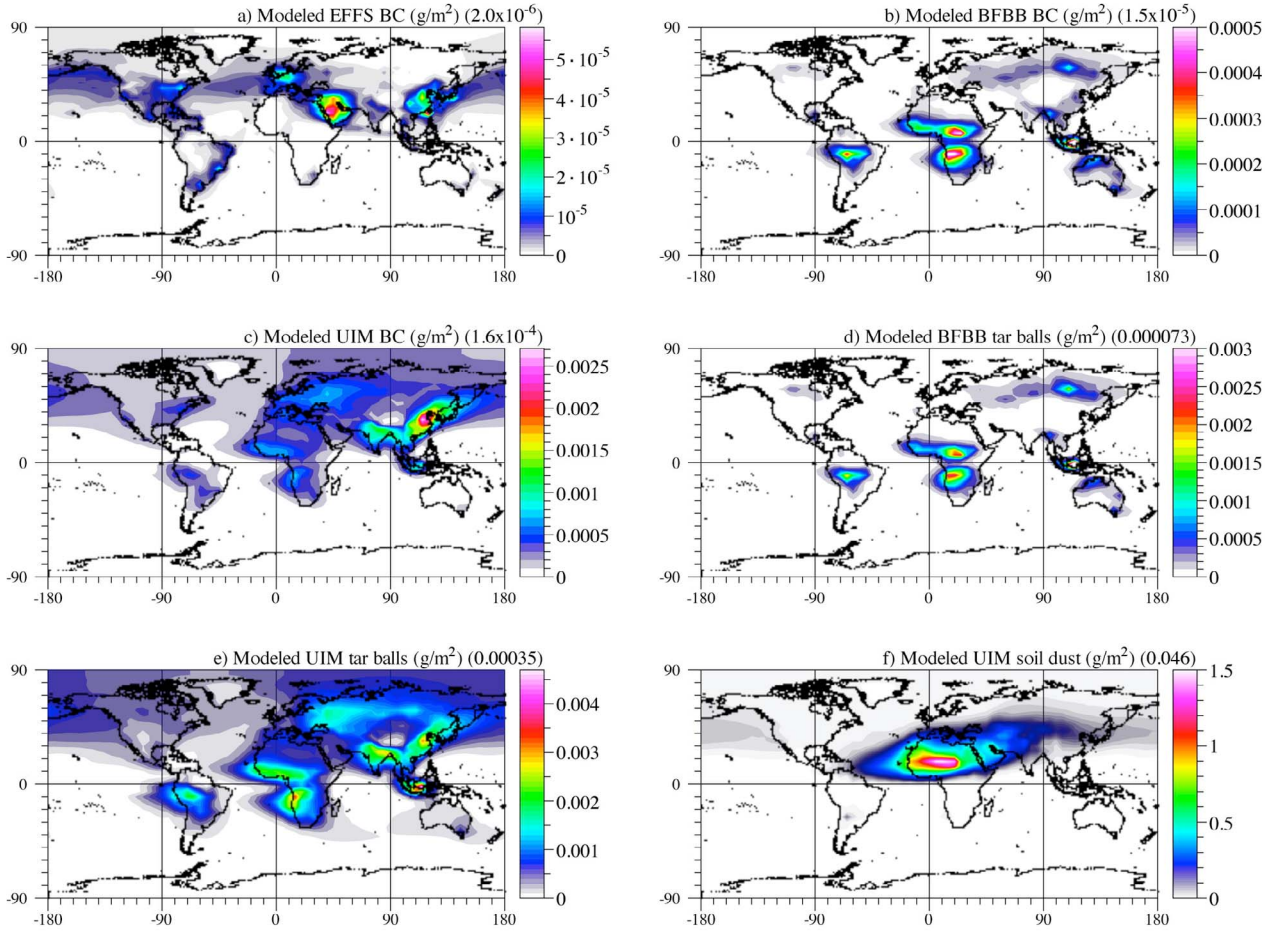

Figure 7. Annually averaged modeled column abundance of BC in the (a) emitted fossil-fuel soot (EFFS), (b) biofuel and biomass burning (BFBB) and (c) ultimate internally mixed (UIM) aerosol size distributions in the model. (d) Same as Figure 7b but for BFBB tar balls. (e) Same as Figure 7c but for UIM tar balls. (f) Same as Figure 7c bur for UIM soil dust.

hydrometeor particles and were either wet removed or stayed in the cloud, affecting the CAOD.

[54] To examine whether the model overpredicts BC, either in the column average or vertical profile, modeled BC vertical profiles were compared with data between 67 S and 80 N over the Pacific from 1–31 January 2009 from the HIPPO campaign [*Schwarz et al.*, 2010] (Figure 11). Model and data column loadings were 67 and 68 mg/m^2, respectively, a 1.4% difference, and the slope of the mean modeled vertical profile was similar to that of the data, indicating little model vertical numerical diffusion in the model. *Schwarz et al.* [2010] compared the same data set against a set of 14 other global models and concluded that such models "overpredicted BC concentrations overall by a factor of 5" and found modeled vertical profile slopes effectively vertical in the troposphere, an indicator of numerical diffusion.

3.5. Mass Absorption Coefficients in the Clear Sky and Between Cloud Particles

[55] In order to understand the impacts of absorbing aerosols and hydrometeor inclusions on climate, it is helpful to quantify the mass absorption coefficients (MAC) for absorbing material in aerosol particles and as inclusions within hydrometeor particles. The MAC (m^2/g) is the ratio of absorption optical depth (dimensionless) to mass loading (g/m^2). Here, the MAC is calculated for BC in aerosol particles (AMAC) and, separately, for BC inclusions in hydrometeor particles (HMAC). The HMAC is also calculated for TB and SD inclusions in hydrometeor particles. For BC in aerosol particles, the AMAC is calculated as if the BC were internally mixed (IM) with a nonabsorbing shell (IM-AMAC) and, separately, externally mixed (EM) (EM-AMAC).

[56] Since the model treated internal mixing of size-resolved BC as it aged among three aerosol size distributions (EFFS, BFBB, and UIM) and since internal mixing caused absorbing material to coat BC, it was necessary to separate out the absorption due to the shell material from the absorption due to the BC core in order to calculate the IM-AMAC of BC. This was done by performing a second Mie calculation each radiation time step during which the imaginary index of refraction of each absorbing shell component of each particle of each size was set to zero. A third Mie calculation was also performed each time step in which the entire coating of BC was removed to determine the EM-AMAC of BC of a given size.

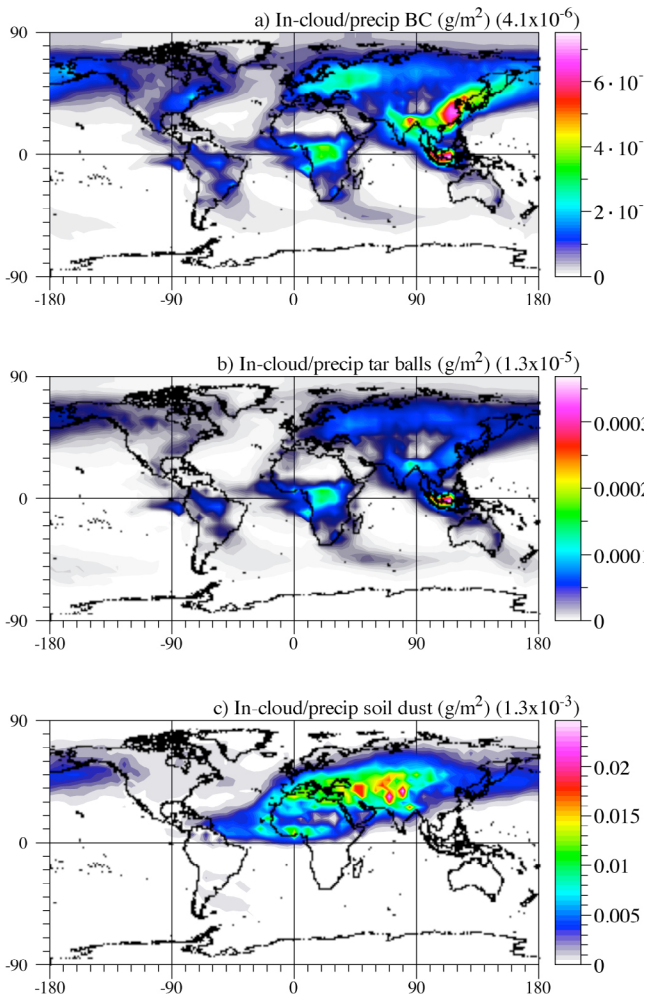

Figure 8. Annually averaged modeled column abundance of (a) BC, (b) tar balls, and (c) soil dust inclusions in liquid, ice, and graupel clouds and precipitation particles. The averages are grid-cell and time averages, so include times and locations with no clouds.

[57] Figure 12 shows the resulting globally distributed annually averaged modeled EM-MAC, IM-AMAC, and the IM-:EM-AMAC ratio of aerosol BC. Aerosol BC is defined as clear-sky BC at the ambient RH plus BC interstitially between hydrometeor particles at the RH of the cloud, but not BC inside of hydrometeor particles. The IM- and EM-AMACs were calculated over the EFFS, BFBB, and UIM aerosol size distributions.

[58] The worldwide spatial distribution of EM-AMAC of BC ranged from 6.3 to 7.3 m^2/g, with a mean of 6.72 m^2/g. This range is within the measured range of 6.3–8.7 m^2/g for uncoated particles suggested by *Bond and Bergstrom* [2006], which was based on a review of the literature. A possible reason for the good match between model and data here is discussed in section 2.5.

[59] The worldwide spatial distribution of IM-AMAC of BC ranged from 13.9–18.2 m^2/g, with a mean of 16.2 m^2/g. The IM-AMAC was greater in cloudy skies than in clear skies due to the higher RH in and near clouds. In humid regions (e.g., at 100% RH), measured mass absorption coefficients can reach 23 m^2/g [*Mikhailov et al.*, 2006, multiplying their EM-AMAC of ~6.6 m^2/g by their maximum amplification factor of 3.5]. Thus, the results in Figure 12b here suggest that modeled coated BC was subject to high RHs in many locations, particularly over the topics and the Arctic. High RHs are expected in much of the world, as shown shortly, since clouds cover most of the world.

3.6. Amplification Factors

[60] The IM-:EM-AMAC ratio, referred to as the *absorption amplification factor*, is an indicator of the enhanced absorption due to internal mixing The annual-average amplification factor of BC ranged globally from 2 to 2.9, with a mean of 2.4. It increased with distance from urban regions and was slightly higher over the ocean than land. The high mean value suggests significant internal mixing and a resulting enhanced absorption by BC. Enhanced absorption on the global scale due to internal mixing of BC has been modeled previously based on size-resolved, time-dependent interactions [*Jacobson*, 2002a, 2004, 2006, 2010].

[61] The range of amplification factors here makes more sense in light of Figure 13, which shows amplification factors of BC cores of different size coated by increasing S(VI) shells material. The factors were calculated with the Mie code used here for the global simulations. The figure indicates that peak amplification factors ranged from 2.5 to 4, depending on initial BC size. The peak was lowest (2.5) for the largest-sized uncoated BC particle (120 nm diameter) and was greater for smaller initial particles (40 nm and 80 nm). This range is the same as the theoretical peak range of 2.5–4 derived for BC with a nonabsorbing shell in the work of *Fuller et al.* [1999]. The range also encompasses the peak measured amplification factor of 3.5 for a soot-water drop mixture at 100% RH, measured by *Mikhailov et al.* [2006]. For practical applications in a cloud, *Chýlek et al.* [1996] found an amplification factor of BC inclusions within a single drop of 2–2.5, close to the range here of 2–2.9, with a mean of 2.4.

[62] *Schnaiter et al.* [2005] found amplification factors for diesel soot coated by secondary organic aerosol in a laboratory of 1.8–2.1 under subsaturated conditions. *Adler et al.* [2010] found an amplification factor of about 2 for BC coated with organic carbon. *Zhang et al.* [2008] found amplification factors of BC coated by sulfuric acid near 2 at 80% RH relative to freshly emitted particles. *Brem et al.* [2012] found an amplification factor of up to 2.7 at 530 nm for an organic aerosol core resulting from burning oak wood when the RH rose from < 70% to 95%. The amplification factors found here globally are suggestive of coated soot at moderate to high RHs, particularly near and in clouds. The enhanced HMACs of BC inclusions in hydrometeor particles are discussed shortly.

[63] Figure 14 shows that modeled annually averaged RHs at 500 hPa, a typical height of clouds, were highest in the tropics and at high latitudes, similar to data from the AIRS satellite product, also shown. These locations were generally where the greatest amplification factors occurred in Figure 12c. However, some moderately high amplification factors also occurred over some low-RH areas, such as the Sahara. This was because BC over the desert is aged, thus internally mixed with soil dust in the UIM distribution in the model, and soil dust is concentrated over the desert. Since

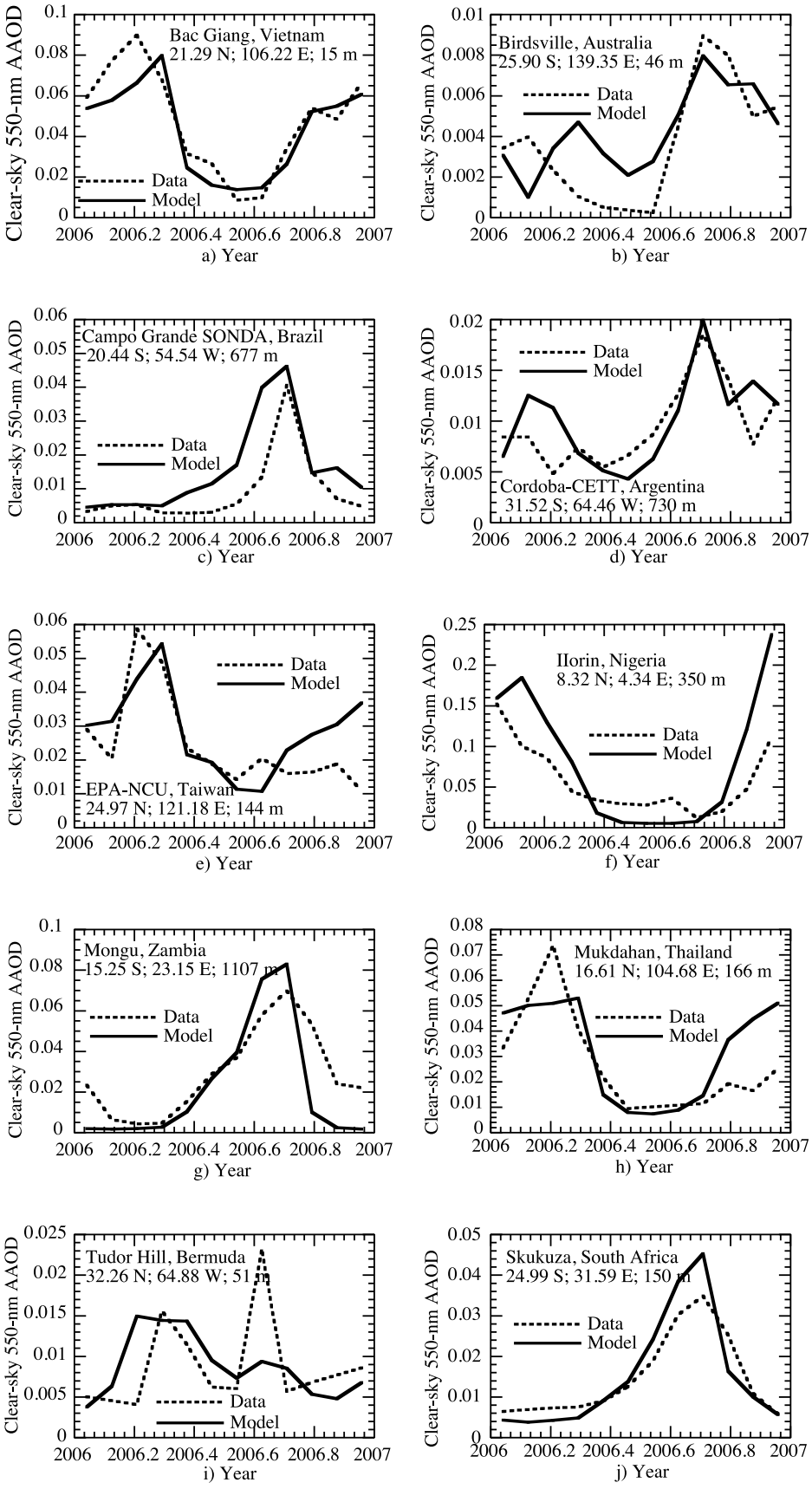
Clear-sky 550-nm AAOD
Bac Giang, Vietnam
21.29 N; 106.22 E; 15 m
Data
Model
a) Year
Birdsville, Australia
25.90 S; 139.35 E; 46 m
b) Year
Campo Grande SONDA, Brazil
20.44 S; 54.54 W; 677 m
c) Year
Cordoba-CETT, Argentina
31.52 S; 64.46 W; 730 m
d) Year
EPA-NCU, Taiwan
24.97 N; 121.18 E; 144 m
e) Year
Ilorin, Nigeria
8.32 N; 4.34 E; 350 m
f) Year
Mongu, Zambia
15.25 S; 23.15 E; 1107 m
g) Year
Mukdahan, Thailand
16.61 N; 104.68 E; 166 m
h) Year
Tudor Hill, Bermuda
32.26 N; 64.88 W; 51 m
i) Year
Skukuza, South Africa
24.99 S; 31.59 E; 150 m
j) Year
2006 2006.2 2006.4 2006.6 2006.8 2007

Figure 9

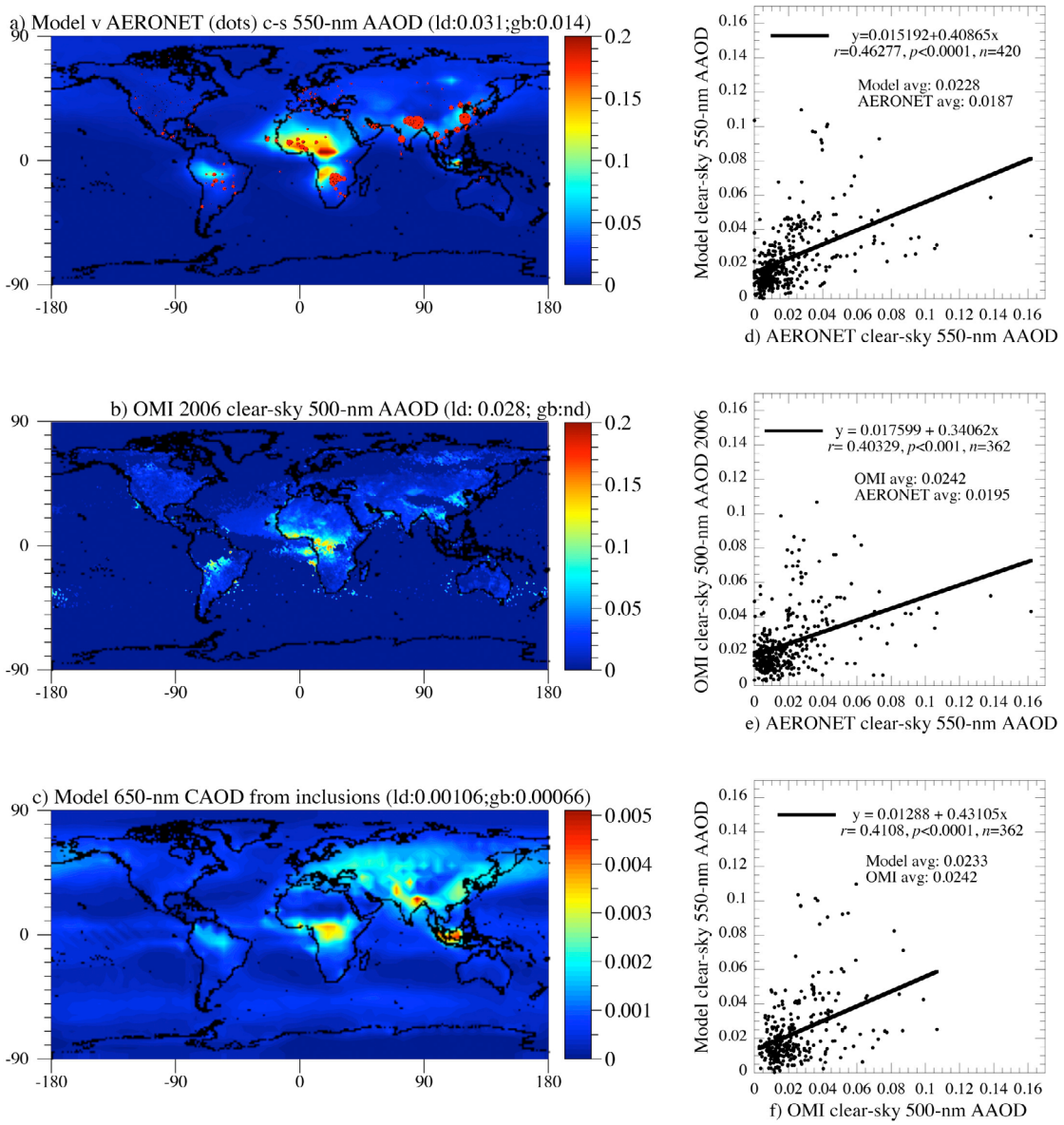

Figure 10. (a) Modeled and AERONET (dots) annually averaged clear-sky 550 nm AAOD at all 420 stations. The dots provide relative values. (d) Magnitudes of the maximum dot sizes, which is a scatterplot of all modeled values at the locations of the measurements in Figure 10a. (b) Annually averaged 2006 OMI 500 nm AAOD [*Torres et al.*, 2007; D. Whitt, personal communication, 2011] Most of the oceans, Arctic, Antarctic, Amazaon, Himalayas, and northern Russia and Canada have zero values. (c) Modeled cloud absorption optical depth at 650 nm due to inclusions within hydrometeor particles only (absorbing aerosols interstitially between hydrometeor particles are part of all-sky AAOD). (e) Scatterplot of multiyear AERONET versus 2006 OMI AAODs at AERONET sites where OMI data were available. (f) Scatterplot of 2006 OMI 500 nm AAOD versus 2006 model AAOD at AERONET sites where OMI data were available.

Figure 9. Comparison of monthly AERONET [*Holben et al.*, 2001] clear-sky total aerosol absorption optical depth (AAOD) at 550 nm, averaged over several years, with model values at 10 locations on four continents and Bermuda. Model values were calculated for 2006 at the location of the station with bilinear interpolation among four surrounding 4° × 5° horizontal resolution grid cells and accounted for absorption by BC, tar balls, other absorbing organics, and soil dust. The data were a derived inversion product, extracted, averaged, and interpolated to 550 nm over each month for several years (S. Kinne, personal communication, 2011).

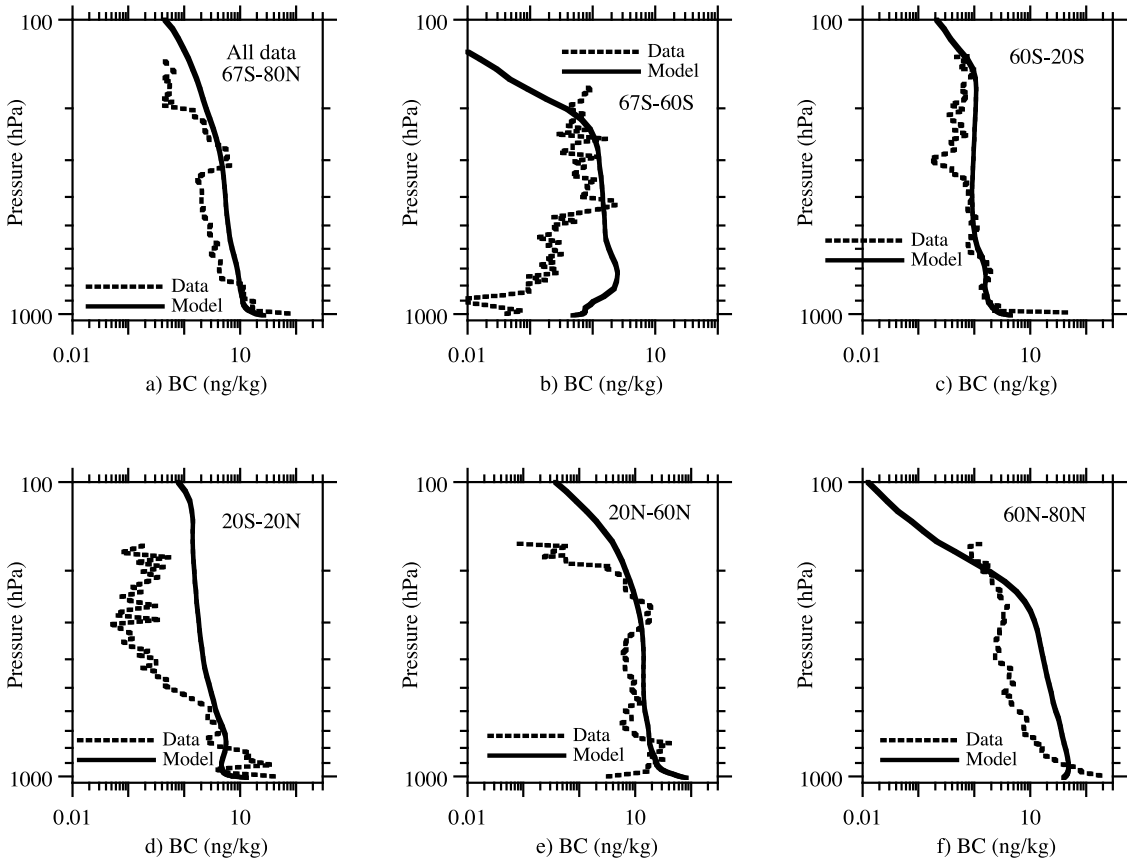

Figure 11. Comparison of GATOR-GCMOM (at 4° × 5° horizontal resolution) modeled black carbon vertical profiles with data between 67°S and 80°N over the Pacific from 1–31 January 2009 from the HIPPO campaign [*Schwarz et al.*, 2010]. Model and data column loadings are 67 and 68 $\mu g/m^2$, respectively, a 1.4% difference.

the model treated this mixture as a BC core (when BC was in the particle) surrounded by a shell, the soil dust amplified the AMAC of BC in a manner similar to liquid water amplifying BC in high-RH locations. Whereas, BC is more likely to be an appendage to rather than a core in a binary soil dust particle, BC in the UIM distribution is also mixed with liquids, such as sulfuric and nitric acid, which likely create amorphous-shaped mixtures together with soil dust.

3.7. Hydrometeor Particle Inclusion MACs (HMACs)

[64] Figure 15 shows the global distribution of the annually averaged modeled 650 nm HMAC of BC inclusions in liquid, ice, and graupel cloud and precipitation particles. The mean value was 17.7 m^2/g, with a range of 12–19.5 m^2/g. The mean was about 9.3% higher than the IM-AMAC for aerosol BC in the clear sky and interstitially between hydrometeor particles (Figure 12b). The reason for the higher HMACs than IM-AMACs is that cloud and precipitation particles have larger shells than do aerosol particles at high RH, and the larger the shell, the larger the amplification factor up to a point (Figure 13). The range in annually averaged modeled HMACs was still much lower than the highest possible measured MAC of BC surrounded by a water shell at 100% RH, 23 m^2/g [*Mikhailov et al.*, 2006].

[65] The spatial distribution of the HMAC of BC was relatively uniform globally, with only pockets of low values, mostly over regions of low RH (Figure 14), and over the Antarctic.

[66] The spatial distribution of the modeled 650 nm HMAC of soil dust inclusions in hydrometeor particles was very similar to that of BC, because the HMAC depends primarily on the size of cloud and precipitation particles, and BC and soil dust were both inclusions in many of the same hydrometeor particles. As such, a figure for soil dust is not shown. However, the mean cloud-particle-inclusion HMAC of soil dust (0.093 m^2/g) was about 1/190th that of BC at 650 nm.

[67] The 650 nm HMAC of tar balls ranged from 6.4 to 10.4, with a mean of 9.4, about half the HMAC of BC. The spatial distribution was also similar to those of BC and soil dust. The high HMAC for tar balls occurred for two reasons. First, the imaginary refractive index of tar balls from available data at 650 nm was about 35% that of BC (Figure 1). Second, pure tar balls are larger than soot particles, and their single-particle absorption efficiency is closer to their peak absorption efficiency than are soot particles. Thus, the lower imaginary refractive index of TBs was partly compensated for by the higher absorption efficiency to give TBs a HMAC about half that of BC. Although the imaginary refractive index data for tar balls is still uncertain and variable, these are the only data currently available to examine this issue with.

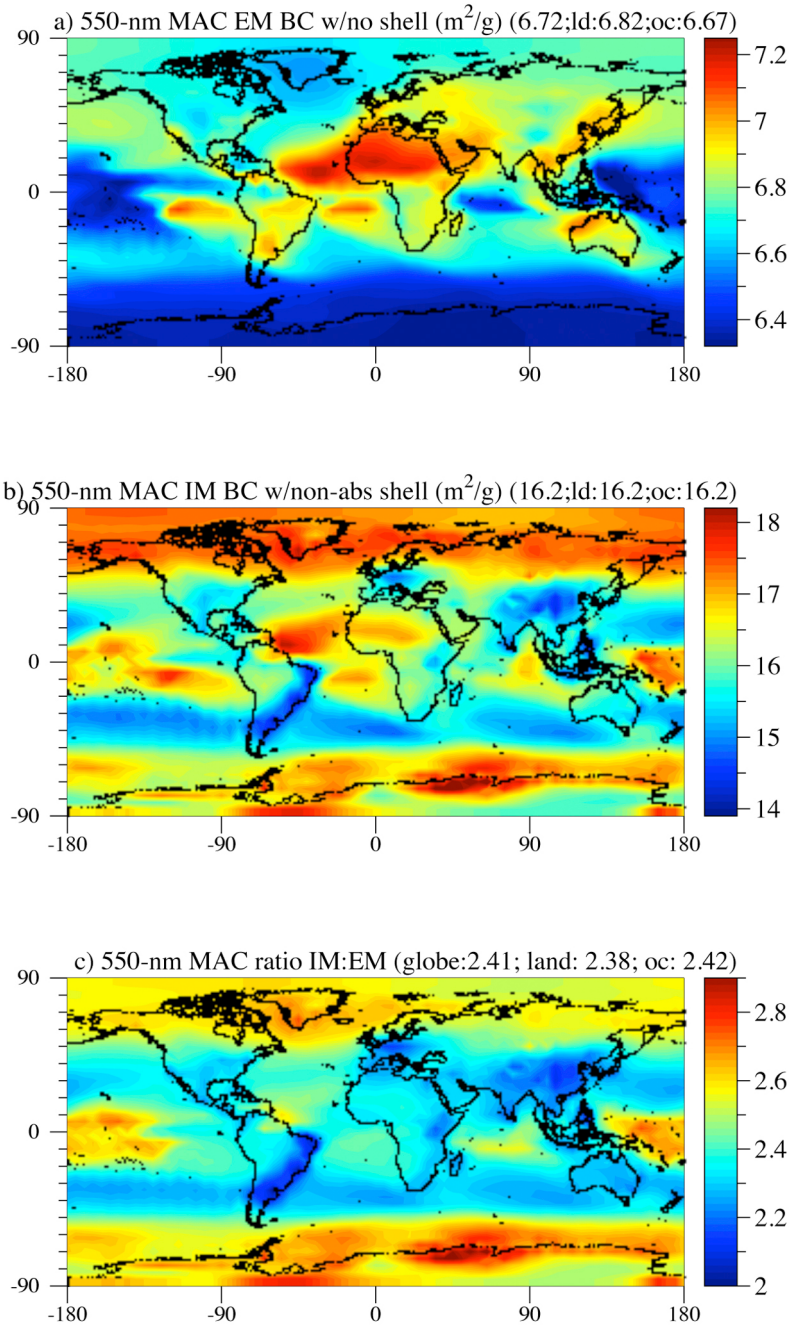

Figure 12. (a) Annually averaged modeled mass-absorption coefficients (MAC) of externally mixed aerosol BC in the clear sky and interstitially between cloud drops at the RH of the cloud, but not inside of cloud drops. The results were obtained by calculating the aerosol absorption optical depth (AAOD) for each aerosol size in each of the three aerosol size distributions assuming a BC core with the shell removed. (b) Annually averaged modeled MAC of internally mixed BC, obtained by calculating the AAOD as in Figure 12a but including the modeled mixed shell composition with the shell imaginary refractive index set to zero to eliminate the impacts of absorbing species aside from BC on the MAC, and (c) the BC amplification factor, which is the ratio of the internally mixed to externally mixed MACs of aerosol BC at 550 nm.

3.8. Heating Rates in Cloud Inclusions, Interstitially, and in the Clear Sky

[68] A 1-D version of GATOR-GCMOM was run with specified vertical profiles of cloud liquid water and BC mass to examine heating rates due to different optical treatments of BC. Figures 16b, 16d, 16f, and 16h compare heating rates for four types of clouds (low, medium, cirrus, and vertically developed) resulting from each of five treatments of BC absorption given the initial profiles in Figures 16a, 16c, 16e,

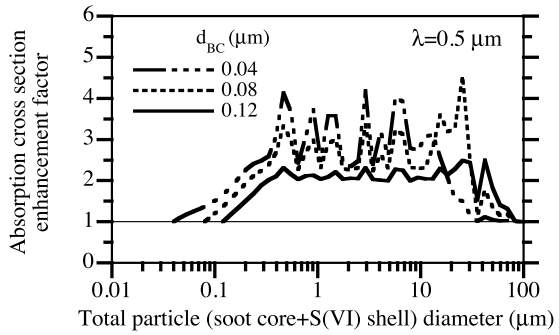

Figure 13. Mie-calculated absorption cross-section enhancement factors, which are equivalent to amplification factors. The enhancement factor is the ratio of the absorption cross section of a total particle with a BC core (either 40, 80, or 120 nm diameter) plus an S(VI) shell to the larger of the absorption cross section of BC alone (at either 40, 80, or 120 nm diameter) or of pure S(VI) at the same size as the total core plus shell particle (which affects the factor only at large sizes). The leftmost values in the panel are the enhancement factor (1.0) corresponding to the pure core. The rightmost values (1.0) are those corresponding to a large pure S(VI) drop that absorbs since all particles with a nonzero imaginary refractive index become absorbing at some size. The Mie code used was from *Ackerman and Toon* [1981]. Figure from *Jacobson* [2003b].

and 16g, respectively. The five treatments of BC absorption included three treatments of BC inclusions in hydrometeor particles, one treatment of BC interstitially between hydrometeor particles, and one case of BC in the clear sky in the absence of the clouds. BC in aerosol and the clear sky were coated with both soluble and insoluble material (Table 1). Inside the cloud, hydration of liquid water to the interstitial aerosol was calculated from thermodynamic equilibrium at RH = 99.99%, accounting for all solutes in solution; outside the cloud, hydration was calculated from the ambient RH profile, which ranged from 65% near the surface to 13% in the middle troposphere.

[69] Particle inclusions within hydrometeor particles for the figure were simulated with either the DEMA (with two maximum inclusion sizes) or the CSA. As discussed (section 2.4), the DEMA is arguably the more physical representation. Figure 1 of *Jacobson* [2006] illustrates that, for a specific-sized cloud drop, the single-particle absorption efficiency is larger for most visible wavelengths with the DEMA approximation than with the CSA approximation. For low, mid-height, and thick hydrometeor size distributions here, this was also found to be the case (Figures 16b, 16d, and 16h), as DEMA:CSA peak heating rate ratios ranged from 1.45 to 3.6:1. However, for the cirrus (or contrail) cloud, the DEMA:CSA heating rate ratio was near unity (Figure 16e), since so little BC existed in these clouds that the sizes and numbers of inclusions were small.

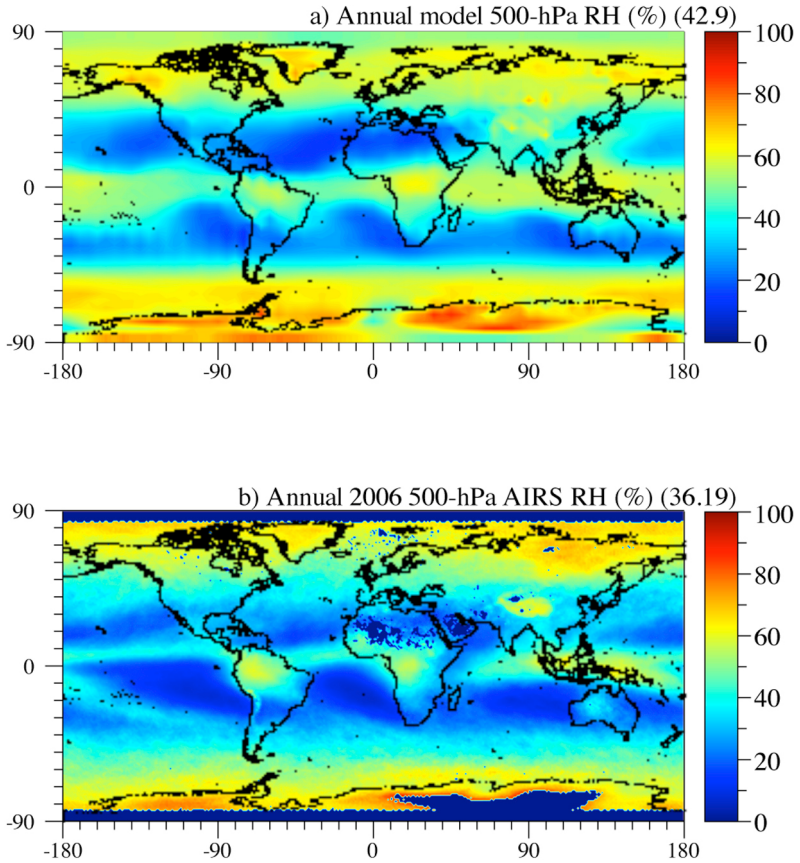

Figure 14. Comparison of (a) modeled with (b) satellite-derived 500 hPa annually averaged 2006 RH, obtained from the Atmospheric Infrared Sounder (AIRS) [*Parkinson et al.*, 2003].

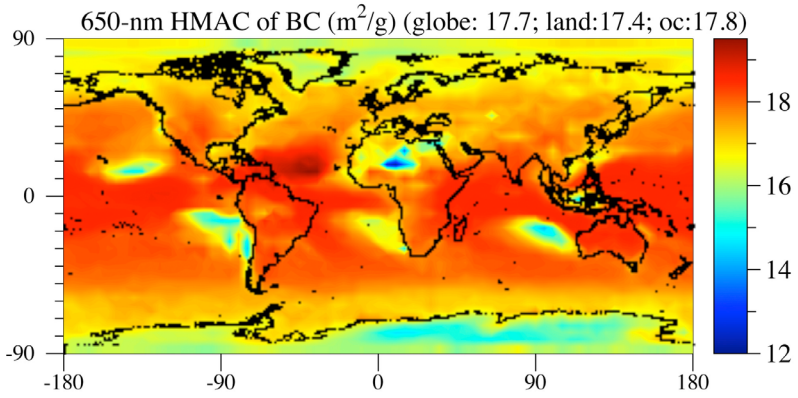

Figure 15. Annually averaged modeled 650 nm hydrometeor mass absorption coefficient (HMAC) of BC inclusions in liquid, ice, and graupel cloud and precipitation particles. The HMAC does not account for the mass absorption coefficient of aerosol particles interstitially between hydrometeor particles or outside of clouds, which were accounted for in Figure 12.

[70] Peak cloud heating rates with the DEMA were 1.7–3 times those of BC interstitially between hydrometeor particles for low, mid, and thick clouds (Figures 16b, 16d, and 16h) and 5 times those of interstitial BC for the cirrus (or contrail) cloud (Figure 16f). The stronger heating rate due to BC inclusions than due to interstitial BC was due to the fact that hydrometeor particles received not only multiple-scattered light from other hydrometeor particles (as did interstitial particles) but also light that refracted into the particle that they resided in. Light refracted into a hydrometeor particle then internally reflected multiple times, increasing the chance it would hit a BC inclusion. Much less absorption occurred for interstitial BC in the cirrus case because fewer hydrometeor particles were present to scatter light to the interstitial BC in that case than in the other cases. In the case of cirrus clouds, the interstitial RH is often closer to the saturation point over ice than that over liquid. Despite the lower water uptake by BC-containing particles at the saturation point over ice than over liquid, interstitial BC still absorbs strongly at the saturation point over ice due to the strong multiple scattering by ice crystals that the BC encounters.

[71] In the low-cloud case, peak cloud heating rates with the DEMA were 5–8 times those of clear-sky BC at the same height as the DEMA peak (near cloud top) but only 3–6 times those of clear-sky BC at the height of the peak clear-sky BC heating rate (near the surface) (Figure 16b). In the mid-cloud case, peak cloud heating rates with the DEMA were 6–9 times those of clear-sky BC at the same height as the DEMA peak and 2–3 times those of clear-sky BC at the height of the peak clear-sky BC heating rate (Figure 16d). In the cirrus (contrail) cloud case, the peak heatings rate with the DEMA and CSA were both about 30 times that of the clear-sky heating rate at the same height as the DEMA peak but only 15% of the clear-sky BC heating rate at the height of the clear-sky heating rate.

[72] Thus, the higher the cloud, the greater the ratio of cloud-inclusion absorption to clear-sky absorption at the height of the inclusions, but the lower the ratio of peak cloud-inclusion absorption to peak clear-sky BC absorption. The peak height of clear-sky BC absorption occurred below the cloud. The cirrus case illustrates this result in the extreme. It shows that DEMA heating rates far outweighed clear-sky heating rates at the height of the cirrus but were much lower than were the peak clear-sky heating rate near the surface. Thus, BC inclusions in hydrometeor particles and BC interstitially between hydrometeor particles increased the height of maximum BC heating for the same BC vertical profile, compared with clear-sky BC.

[73] The peak heating rates in Figure 16d (0.10 K/h for DEMA-200, 0.061 K/h for DEMA-100, and 0.042 K/h for CSA) were for a cloud between 0.5 and 3 km altitude. The peaks occurred near the top of the cloud. At that location, the BC volume fraction was about 1×10^{-6}, but it varied vertically in the cloud. *Li et al.* [2011] calculated a similar vertical heating rate profile and a peak heating rate of about 0.045 K/d for a low cloud between 1 and 2 km when a constant volume fraction of 1×10^{-6} BC throughout the cloud and a well-mixed parameterization of BC absorption in cloud drops were used. Although the cloud thicknesses

Figure 16. Liquid or ice water content (LWC), black carbon (BC) profiles, and solar heating rates due to BC for (a and b) low, (c and d) middle, (e and f) cirrus, and (g and h) thick cloud. Each heating rate figure shows results for five cases: (1) aerosol (including BC) in the clear sky ("aerosol without cloud") (in this cases, the BC profile in Figure 16a is the same as the cloudy-sky BC profile); (2) the same aerosol interstitially between cloud hydrometeor particles with aerosol water determined at 100% RH plus aerosol above and below the cloud at the ambient RH ("aerosol in cloud between drops"); (3) the same aerosol treated as inclusions randomly distributed within cloud drops using the DEMA with maximum inclusion diameter of 100 nm ("aerosol in drops-DEMA-100 nm"); (4) the same as (3) but with maximum inclusion diameter of 200 nm; and (5) the same aerosol treated as hydrometeor inclusions with the CSA ("aerosol in drops–CSA"). The total column abundance of BC was 0.00253 g/m^2 in all cases. The calculations were at 12:00 GMT, 1 January 2006 at 10°S, 20°E. The zenith angle was 22.86°. For Figure 16b, the BC volume fraction ranged from 2.7×10^{-6} at the base to 7×10^{-7} at the top of the cloud.

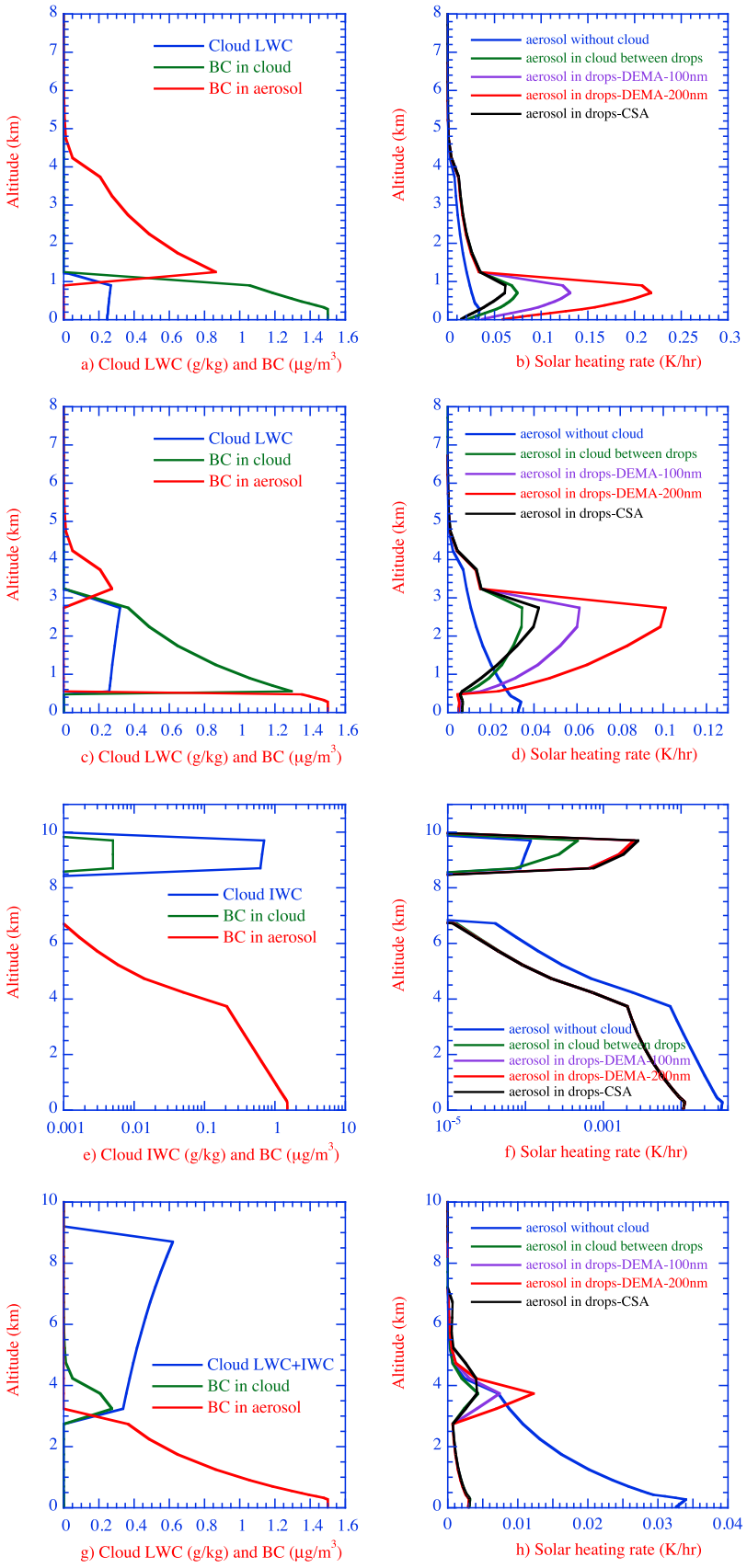
Cloud LWC
BC in cloud
BC in aerosol
Altitude (km)
a) Cloud LWC (g/kg) and BC (μg/m3)
aerosol without cloud
aerosol in cloud between drops
aerosol in drops-DEMA-100nm
aerosol in drops-DEMA-200nm
aerosol in drops-CSA
b) Solar heating rate (K/hr)
c) Cloud LWC (g/kg) and BC (μg/m3)
d) Solar heating rate (K/hr)
Cloud IWC
e) Cloud IWC (g/kg) and BC (μg/m3)
f) Solar heating rate (K/hr)
Cloud LWC+IWC
g) Cloud LWC (g/kg) and BC (μg/m3)
h) Solar heating rate (K/hr)

Figure 16

Table 4. Ratio of Column-Integrated Heating Rate due to BC Between Pairs of Absorption Treatments for Each Cloud Type in Figure 16[a]

Cloud Type	DEMA:CSA	DEMA:ISC	DEMA:Clear	CSA:Clear	ISC:Clear	ISC:ISA
Low (Figure 16b)	2.30	2.03	3.69	1.60	1.81	1.17
Mid (Figure 16d)	2.25	2.35	2.84	1.26	1.21	1.27
Cirrus (Figure 16f)	0.99	1.04	0.31	0.31	0.30	1.03
Thick (Figure 16h)	1.36	1.65	0.21	0.16	0.13	1.18

[a]The ratio of column-integrated heating rate due to BC is the product of heating rate, air density, and layer thickness, summed over all layers, and divided by the summed product of air density and layer thickness. DEMA = Dynamic effective medium approximation with maximum inclusion diameter of 200-nm; CSA = core-shell approximation; ISC = BC interstitially between hydrometeor particles at ~100% RH; ISA = BC interstitially between hydrometeor particles at the RH of clear-sky BC; Clear = BC in the clear sky.

and absorption treatment differed between the simulations and *Li et al.* did not treat the DEMA in their calculation, the magnitude of the peak heating rate from that study was still close to the CSA result from the present study.

[74] Table 4 compares ratios of the column-integrated heating rate when one approximation versus another was used to represent BC heating for each cloud type. The table shows that, for low and mid clouds, BC inclusions resulted in column-integrated BC heating rates of 203% and 235%, respectively, those of interstitial BC at the actual cloud RH. Interstitial BC at its actual RH, in turn, resulted in heating rates of 116% and 127%, respectively, that of interstitial BC at the clear-sky RH. Interstitial BC at its actual RH also caused column heating of 181% and 121%, respectively, that of clear-sky aerosol BC outside of the cloud.

[75] Further, column-integrated heating rates due to low- and mid-cloud inclusions resulted in greater overall heating than did clear-sky BC by a factor of 2.8–3.7 for the DEMA and 1.3–1.6 for the CSA. Interstitial BC resulted in 1.2–1.8 times the column heating than did clear-sky BC for the same clouds. BC also impacted column heating for thick clouds but lesser so for cirrus clouds. Nevertheless, BC in all clouds enhanced the heating of the cloud layer compared with no BC. In sum, a model needs to account for the swelling of particles containing BC at the cloud RH and for BC inclusions in hydrometeor particles is necessary to account correctly for the effects of BC on cloud heating.

[76] The implications of Figure 16 are significant. Many papers have simulated the potential effects of BC aerosols above, within, and/or below clouds on the suppression or enhancement of clouds, as summarized in the work of *Koch and Del Genio* [2010]. However, none of the studies treated the BC in clouds as containing hygroscopic material at the RH of the cloud or as inclusions in hydrometeor particles. Instead, they treated it only as if it were interstitially between hydrometeor particles at the clear-sky RH (or with no hygroscopic material). Figure 16 shows an important distinction between the effects of interstitial BC and BC inclusions and of the effects of BC inclusions at the cloud versus ambient RH.

3.9. Global Boomerang Curve

[77] Finally, Figure 17 gives the annually averaged cloud optical depth (COD) in each model column correlated in space with the annually averaged modeled aerosol optical depth (AOD) and, separately, with the annually averaged modeled aerosol absorption optical depth (AAOD). A third-order polynomial is fit through the results in each case. The curves in both cases have the shape of a boomerang, suggesting that, in the global average, COD increased with increasing AOD at low AOD, whereas COD decreased with increasing AOD at high AOD. This result is consistent with high-resolution satellite analyses of cloud optical depth over biomass-burning regions of Brazil [*Ten Hoeve et al.*, 2011] and satellite analyses of cloud fraction [*Koren et al.*, 2008; *Kaufman and Koren*, 2006]. However, the result here uniquely shows that the phenomena may occur on the global scale as well.

[78] The explanation for the boomerang curve is as follows. At low AOD, an increase in aerosol particle number increases COD due to the first indirect (microphysical) effect. At increasing AOD, the cloud absorption and semidirect

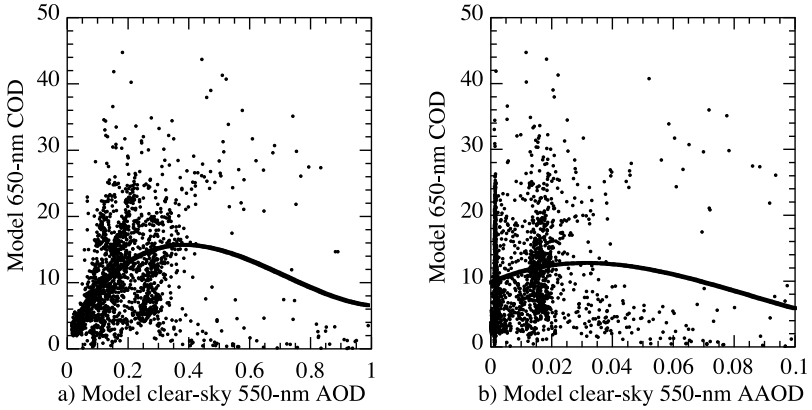

Figure 17. Annually averaged modeled 650 nm cloud optical depth (COD) paired in space with the corresponding 550 nm clear-sky (a) aerosol optical depth (AOD) and (b) aerosol absorption optical depth (AAOD). The solid lines are third-order polynomial fits through the results.

effects (radiative effects) decrease COD. As the microphysical and radiative effects are not linearly additive and both occur to some degree at all AODs, accounting for both together during a model simulation is essential for simulating the role of absorbing material on clouds.

4. Conclusions

[79] This study examined several modeled globally distributed properties of black carbon (BC), tar balls (TB), and soil dust (SD), particularly with respect to their absorption in clouds and the clear sky. The goal was to elucidate better the modeled properties of absorbing aerosol components to understand better cloud absorption effects I and II, which are the effects on cloud heating of absorbing inclusions in hydrometeor particles and of absorbing aerosol particles interstitially between hydrometeor particles at their actual relative humidity (RH), respectively. Model results were also compared with data for some parameters. Key results are as follows:

[80] 1. The annual-average amplification factor of aerosol BC (ratio of the IM:EM-AMAC of BC) due to internal mixing ranged from 2 to 2.9 globally, with a mean of 2.4. Values were highest at high latitudes and in the tropics, where the RH was high. It increased with distance from urban regions and with increasing RH. The high end of the range is much less than the theoretical limit of 4 and one measured value at 100% RH of 3.5.

[81] 2. The AMAC of externally mixed BC fell within a fairly narrow range, 6.3–7.3 m^2/g globally, with a mean of 6.72 m^2/g. This modeled range is within a suggested measured range of 6.3–8.7 m^2/g.

[82] 3. The AMAC of internally mixed BC ranged from 13.9 to 18.2 m^2/g globally, with a mean of 16.2 m^2/g, with the highest values in humid regions. These values are much lower than the measured maximum MAC at 100% RH, of 23 m^2/g.

[83] 4. The 650 nm HMACs of BC inclusions in cloud and precipitation particles ranged from 10.6 to 19 m^2/g globally, with a mean of 17.7 m^2/g, about 9.3% higher than that of IM-AMACs. The higher MAC in hydrometeor particles was due to the greater average coating of such particles than of aerosol particles at high RH.

[84] 5. The 650 nm HMAC of tar balls may be half that of BC based on published refractive index data, whereas that of soil dust may be about 1/190th that of BC.

[85] 6. Based on a test calculation in a column model, BC inclusions in low and mid clouds increased total column-weighted BC heating by 100% and 135%, respectively, compared with BC interstitially between hydrometeor particles at the actual RH of the cloud. For the same clouds, interstitial BC at the actual RH of the cloud increased column heating by 16% and 27%, respectively, compared with interstitial BC at the RH outside of the cloud and 81% and 21%, respectively, compared with clear-sky aerosol BC outside of the cloud. BC also had strong impacts on column heating rates for thick clouds but lesser impacts on cirrus clouds. BC in all clouds enhanced cloud heating compared with no BC.

[86] 7. In the 1-D test case, the overall column weighted heating rate due to treating BC inclusions as polydispere in a cloud particle (DEMA approximation) exceeded that due to treating BC as a single core (CSA approximation) by up to a factor of 2.3 and as interstitial aerosol particles at the RH of the cloud by up to a factor of 2.4.

[87] 8. BC inclusions in cloud particles and BC interstitially between cloud particles increased the height of the maximum heating rate of BC for the same BC vertical profile compared with the clear sky.

[88] 9. The globally averaged all-sky cloud absorption optical depth (CAOD) was about 6.7% that of the clear-sky aerosol absorption optical depth (AAOD) at 650 nm.

[89] 10. Accounting for the swelling of particles containing BC at the cloud RH and for BC inclusions in hydrometeor particles is necessary to account correctly for the effects of BC on cloud heating.

[90] 11. Globally, about 92.6% of BC wet+dry deposition was wet, whereas about 75% of soil dust deposition was wet. Of BC and soil dust that deposited to any snow or sea ice worldwide, only about 0.53% and 2.3%, respectively, dry deposited. Most wet deposition over snow or ice occurred at mid latitudes. Over the Arctic, though about two thirds of both BC and soil dust deposition was wet.

[91] 12. On a global scale, COD first increased with increasing AOD but decreased with a further increase in AOD, consistent with the boomerang curves found in high-resolution satellite and modeling studies. As the microphysical and radiative effects of aerosols on clouds are not linearly additive and both occur to some degree at all AODs, accounting for both together during a model simulation is essential for simulating the role of absorbing material on clouds.

[92] 13.Modeled aerosol absorption optical depths and the vertical profile of BC seem relatively consistent with satellite and aircraft data.

[93] **Acknowledgments.** This work was supported by U.S. Environmental Protection Agency grant RD-83337101-O, NASA grant NX07AN25G, the NASA High-End Computing Program, and the National Science Foundation. We thank Stefan Kinne for processing and providing AERONET data, AERONET PIs for maintaining AERONET sites, and Daniel Whitt for processing OMI data.

References

Ackerman, A. S., O. B. Toon, D. E. Stevens, A. J. Heymsfield, V. Ramanathan, and E. J. Welton (2000), Reduction of tropical cloudiness by soot, *Science*, *288*, 1042–1047, doi:10.1126/science.288.5468.1042.

Ackerman, T. P., and O. B. Toon (1981), Absorption of visible radiation in atmosphere containing mixtures of absorbing and nonabsorbing particles, *Appl. Opt.*, *20*, 3661–3667, doi:10.1364/AO.20.003661.

Adachi, K., and P. R. Buseck (2011), Atmospheric tar balls from biomass burning in Mexico, *J. Geophys. Res.*, *116*, D05204, doi:10.1029/2010JD015102.

Adler, G., A. A. Riziq, C. Erlick, and Y. Rudich (2010), Effects of intrinsic organic carbon on the optical properties of fresh diesel soot, *Proc. Natl. Acad. Sci. U. S. A.*, *107*, 6699–6704, doi:10.1073/pnas.0903311106.

Alexander, D. T. L., P. A. Crozier, and J. R. Anderson (2008), Brown carbon spheres in East Asian outflow and their optical properties, *Science*, *321*, 833–836, doi:10.1126/science.1155296.

Andreae, M. O., and P. Merlet (2001), Emission of trace gases and aerosols from biomass burning, *Global Biogeochem. Cycles*, *15*, 955–966, doi:10.1029/2000GB001382.

Andreae, M. O., D. Rosenfeld, P. Artaxo, A. A. Costa, G. P. Frank, K. M. Longo, and M. Z. F. Silva-Dias (2004), Smoking rain clouds over the Amazon, *Science*, *303*, 1337–1342, doi:10.1126/science.1092779.

Bond, T. C., and R. W. Bergstrom (2006), Light absorption by carbonaceous particles: An investigative review, *Aerosol Sci. Technol.*, *40*, 27–67, doi:10.1080/02786820500421521.

Bond, T. C., D. G. Streets, K. F. Yarber, S. M. Nelson, J.-H. Woo, and Z. Klimont (2004), A technology-based global inventory of black and

organic carbon emissions from combustion, *J. Geophys. Res.*, *109*, D14203, doi:10.1029/2003JD003697.

Brem, B. T., F. C. Mena Gonzalez, S. R. Meyers, T. C. Bond, and M. J. Rood (2012), Laboratory-measured optical properties of inorganic and organic aerosol at relative humidities up to 95%, *Aerosol Sci. Technol.*, *46*, 178–190, doi:10.1080/02786826.2011.617794.

Chen, J., J. C. Wenger, and D. S. Venables (2011), Near-ultraviolet absorption cross sections of nitrophenols and their potential influence on tropospheric oxidation capacity, *J. Phys. Chem. A*, *115*, 12,235–12,242, doi:10.1021/jp206929r.

Chuang, C. C., J. E. Penner, J. M. Prospero, K. E. Grant, G. H. Rau, and K. Kawamoto (2002), Cloud susceptibility and the first aerosol indirect forcing: Sensitivity to black carbon and aerosol concentrations, *J. Geophys. Res.*, *107*(D21), 4564, doi:10.1029/2000JD000215.

Chýlek, P., V. Ramaswamy, and R. J. Cheng (1984), Effect of graphitic carbon on the albedo of clouds, *J. Atmos. Sci.*, *41*, 3076–3084, doi:10.1175/1520-0469(1984)041<3076:EOGCOT>2.0.CO;2.

Chýlek, P., G. B. Lesins, G. Videen, J. G. D. Wong, R. G. Pinnick, D. Ngo, and J. D. Klett (1996), Black carbon and absorption of solar radiation by clouds, *J. Geophys. Res.*, *101*, 23,365–23,371, doi:10.1029/96JD01901.

Conant, W. C., A. Nenes, and J. H. Seinfeld (2002), Black carbon radiative heating effects on cloud microphysics and implications for the aerosol indirect effect: 1. Extended Köhler theory, *J. Geophys. Res.*, *107*(D21), 4604, doi:10.1029/2002JD002094.

Danielson, R. E., D. R. Moore, and H. C. van de Hulst (1969), The transfer of visible radiation through clouds, *J. Atmos. Sci.*, *26*, 1078–1087, doi:10.1175/1520-0469(1969)026<1078:TTOVRT>2.0.CO;2.

Erlick, C., V. Ramaswamy, and L. M. Russell (2006), Differing regional responses to a perturbation in solar cloud absorption in the SKYHI general circulation model, *J. Geophys. Res.*, *111*, D06204, doi:10.1029/2005JD006491.

Ferek, R. J., J. S. Reid, P. V. Hobbs, D. R. Blake, and C. Liousse (1998), Emission factors of hydrocarbons, halocarbons, trace gases, and particles from biomass burning in Brazil, *J. Geophys. Res.*, *103*, 32,107–32,118, doi:10.1029/98JD00692.

Flores, J. M., R. Z. Bar-Or, N. Bluvshtein, A. Abo-Riziq, A. Kostinski, S. Borrmann, I. Koren, and Y. Rudich (2012), Absorbing aerosols at high relative humidity: Closure between hygroscopic growth and optical properties, *Atmos. Phys. Chem. Discuss.*, *12*, 1019–1052, doi:10.5194/acpd-12-1019-2012.

Forster, P., et al. (2007), Changes in atmospheric constituents and in radiative forcing, in *Climate Change 2007: The Physical Science Basis. Contribution of Working Group I to the Fourth Assessment Report of the Intergovernmental Panel on Climate Change*, edited by S. Solomon et al., pp. 129–234, Cambridge Univ. Press, New York.

Fukushima, H., Y. Hagihara, H. Kobayashi, T. Murayama, S. Ohta, and I. Uno (2003), Optical model of Asian dust aerosol and its evaluation through SeaWiFS data, paper presented at 2nd International Workshop on Mineral Dust, Cent. Natl. de la Rech. Sci., Paris, 12 Sep.

Fuller, K. A., W. C. Malm, and S. M. Kreidenweis (1999), Effects of mixing on extinction by carbonaceous particles, *J. Geophys. Res.*, *104*, 15,941–15,954, doi:10.1029/1998JD100069.

Giglio, L., G. R. van der Werf, J. T. Randerson, G. J. Collatz, and P. Kasibhatla (2006), Global estimation of burned area using MODIS active fire observations, *Atmos. Chem. Phys.*, *6*, 957–974, doi:10.5194/acp-6-957-2006.

Gillette, D. A., E. M. Patterson Jr., J. M. Prospero, and M. L. Jackson (1993), Soil aerosols, in *Aerosol Effects on Climate*, edited by S. G. Jennings, pp. 73–109, Univ. of Ariz. Press, Tucson.

Grenfell, T. C., and S. G. Warren (1999), Representation of a nonspherical ice particle by a collection of independent spheres for scattering and absorption of radiation, *J. Geophys. Res.*, *104*, 31,697–31,709, doi:10.1029/1999JD900496.

Gunn, R., and B. B. Phillips (1957), An experimental investigation of the effect of air pollution on the initiation of rain, *J. Meteorol.*, *14*, 272–280, doi:10.1175/1520-0469(1957)014<0272:AEIOTE>2.0.CO;2.

Hansen, J., M. Sato, and R. Ruedy (1997), Radiative forcing and climate response, *J. Geophys. Res.*, *102*, 6831–6864, doi:10.1029/96JD03436.

Holben, B. N., et al. (2001), An emerging ground-based aerosol climatology: Aerosol optical depth from AERONET, *J. Geophys. Res.*, *106*, 12,067–12,097, doi:10.1029/2001JD900014.

Jacobson, M. Z. (1998), Improvement of SMVGEAR II on vector and scalar machines through absolute error tolerance control, *Atmos. Environ.*, *32*, 791–796, doi:10.1016/S1352-2310(97)00315-4.

Jacobson, M. Z. (1999), Isolating nitrated and aromatic aerosols and nitrated aromatic gases as sources of ultraviolet light absorption, *J. Geophys. Res.*, *104*, 3527–3542, doi:10.1029/1998JD100054.

Jacobson, M. Z. (2000), A physically based treatment of elemental carbon optics: Implications for global direct forcing of aerosols, *Geophys. Res. Lett.*, *27*, 217–220, doi:10.1029/1999GL010968.

Jacobson, M. Z. (2001a), Global direct radiative forcing due to multicomponent anthropogenic and natural aerosols, *J. Geophys. Res.*, *106*, 1551–1568, doi:10.1029/2000JD900514.

Jacobson, M. Z. (2001b), GATOR-GCMM: A global-through urban-scale air pollution and weather forecast model: 1. Model design and treatment of subgrid soil, vegetation, roads, rooftops, water, sea ice, and snow, *J. Geophys. Res.*, *106*, 5385–5401, doi:10.1029/2000JD900560.

Jacobson, M. Z. (2002a) Control of fossil-fuel particulate black carbon and organic matter, possibly the most effective method of slowing global warming, *J. Geophys. Res.*, *107*(D19), 4410, doi:10.1029/2001JD001376.

Jacobson, M. Z. (2002b) Analysis of aerosol interactions with numerical techniques for solving coagulation, nucleation, condensation, dissolution, and reversible chemistry among multiple size distributions, *J. Geophys. Res.*, *107*(D19), 4366, doi:10.1029/2001JD002044.

Jacobson, M. Z. (2003a), Development of mixed-phase clouds from multiple aerosol size distributions and the effect of the clouds on aerosol removal, *J. Geophys. Res.*, *108*(D8), 4245, doi:10.1029/2002JD002691.

Jacobson, M. Z. (2003b), Reply to comment by J. Feichter et al. on "Control of fossil-fuel particulate black carbon and organic matter, possibly the most effective method of slowing global warming," *J. Geophys. Res.*, *108*(D24), 4768, doi:10.1029/2002JD003299.

Jacobson, M. Z. (2004), The climate response of fossil-fuel and biofuel soot, accounting for soot's feedback to snow and sea ice albedo and emissivity, *J. Geophys. Res.*, *109*, D21201, doi:10.1029/2004JD004945.

Jacobson, M. Z. (2005), A refined method of parameterizing absorption coefficients among multiple gases simultaneously from line-by-line data, *J. Atmos. Sci.*, *62*, 506–517, doi:10.1175/JAS-3372.1.

Jacobson, M. Z. (2006), Effects of absorption by soot inclusions within clouds and precipitation on global climate, *J. Phys. Chem.*, *110*, 6860–6873, doi:10.1021/jp056391r.

Jacobson, M. Z. (2010), Short-term effects of controlling fossil-fuel soot, biofuel soot and gases, and methane on climate, Arctic ice, and air pollution health, *J. Geophys. Res.*, *115*, D14209, doi:10.1029/2009JD013795.

Jacobson, M. Z., and J. H. Seinfeld (2004), Evolution of nanoparticle size and mixing state near the point of emission, *Atmos. Environ.*, *38*, 1839–1850, doi:10.1016/j.atmosenv.2004.01.014.

Jacobson, M. Z., and D. G. Streets (2009), The influence of future anthropogenic emissions on climate, natural emissions, and air quality, *J. Geophys. Res.*, *114*, D08118, doi:10.1029/2008JD011476.

Jacobson, M. Z., and J. E. Ten Hoeve (2012), Effects of urban surfaces and white roofs on global and regional climate, *J. Clim.*, *25*, 1028–1044, doi:10.1175/JCLI-D-11-00032.1.

Jacobson, M. Z., Y. J. Kaufmann, and Y. Rudich (2007), Examining feedbacks of aerosols to urban climate with a model that treats 3-D clouds with aerosol inclusions, *J. Geophys. Res.*, *112*, D24205, doi:10.1029/2007JD008922.

Jacobson, M. Z., J. T. Wilkerson, A. D. Naiman, and S. K. Lele (2011), The effects of aircraft on climate and pollution. Part I: Numerical methods for treating the subgrid evolution of discrete size- and composition-resolved contrails from all commercial flights worldwide, *J. Comput. Phys.*, *230*, 5115–5132, doi:10.1016/j.jcp.2011.03.031.

Johnson, B. T. (2005), The semidirect aerosol effect: Comparison of a single-column model with large eddy simulation for marine stratocumulus, *J. Clim.*, *18*, 119–130, doi:10.1175/JCLI-3233.1.

Kahnert, M. (2010), On the discrepancy between modeled and measured mass absorption cross sections of light absorbing carbon aerosols, *Aerosol Sci. Technol.*, *44*, 453–460, doi:10.1080/02786821003733834.

Kaufman, Y. J., and I. Koren (2006), Smoke and pollution aerosol effect on cloud cover, *Science*, *313*, 655–658, doi:10.1126/science.1126232.

Kirchstetter, T. W., T. Novakov, and P. V. Hobbs (2004), Evidence that spectral light absorption by aerosols emitted from biomass burning and motor vehicles is different due to organic carbon, *J. Geophys. Res.*, *109*, D21208, doi:10.1029/2004JD004999.

Koch, D., and A. D. Del Genio (2010), Black carbon semi-direct effects on cloud cover: Review and synthesis, *Atmos. Chem. Phys.*, *10*, 7685–7696, doi:10.5194/acp-10-7685-2010.

Koren, I., J. V. Martins, L. A. Remer, and H. Afargan (2008), Smoke invigoration versus inhibition of clouds over the Amazon, *Science*, *321*, 946–949, doi:10.1126/science.1159185.

Krekov, G. M. (1993), Models of atmospheric aerosols, in *Aerosol Effects on Climate*, edited by S. G. Jennings, pp. 9–72, Univ. of Ariz. Press, Tucson.

Li, J., E. Mlawer, and P. Chýlek (2011), Parameterization of cloud optical properties for semidirect radiative forcing, *J. Geophys. Res.*, *116*, D23212, doi:10.1029/2011JD016611.

Ludwig, J., L. T. Marufu, B. Huber, M. O. Andreae, and G. Helas (2003), Domestic combustion of biomass fuels in developing countries: A major source of atmospheric pollutants, *J. Atmos. Chem.*, *44*, 23–37, doi:10.1023/A:1022159910667.

Mikhailov, E. F., S. S. Vlasenko, I. A. Podgorny, V. Ramanathan, and C. E. Corrigan (2006), Optical properties of soot-water drop agglomerates: An experimental study, *J. Geophys. Res.*, *111*, D07209, doi:10.1029/2005JD006389.

Moffet, R. C., and K. A. Prather (2009), In-situ measurements of the mixing state and optical properties of soot with implications for radiative forcing estimates, *Proc. Natl. Acad. Sci. U. S. A.*, *106*, 11,872–11,877, doi:10.1073/pnas.0900040106.

Parkinson, C., et al. (2003), Aqua: An Earth-observing satellite mission to examine water and other climate variables, *IEEE Trans. Geosci. Remote Sens.*, *41*, 173–183, doi:10.1109/TGRS.2002.808319.

Pósfai, M., A. Gelencsér, R. Simonics, K. Arató, J. Li, P. V. Hobbs, and P. R. Buseck (2004), Atmospheric tar balls: Particles from biomass and biofuel burning, *J. Geophys. Res.*, *109*, D06213, doi:10.1029/2003JD004169.

Ramanathan, V., and M. V. Ramana (2005), Persistent, widespread, and strongly absorbing haze over the Himalayan foothills and the Indo-Gangetic Plains, *Pure Appl. Geophys.*, *162*, 1609–1626, doi:10.1007/s00024-005-2685-8.

Reddy, M. S., O. Boucher, N. Bellouin, M. Schulz, Y. Balkanski, J.-L. Dufresne, and M. Pham (2005), Estimates of global multicomponent aerosol optical depth and direct radiative perturbation in the Laboratoire de Météorologie Dynamique general circulation model, *J. Geophys. Res.*, *110*, D10S16, doi:10.1029/2004JD004757.

Sandu, I., P. Tulet, and J.-L. Brenguier (2005), Parameterization of the cloud droplet single scattering albedo based on aerosol chemical composition for LES modeling of boundary layer clouds, *Geophys. Res. Lett.*, *32*, L19814, doi:10.1029/2005GL023994.

Sato, M., J. Hansen, D. Koch, A. Lacis, R. Ruedy, O. Dubovik, B. Holben, M. Chin, and T. Novakov (2003), Global atmospheric black carbon inferred from AERONET, *Proc. Natl. Acad. Sci. U. S. A.*, *100*, 6319–6324, doi:10.1073/pnas.0731897100.

Schnaiter, M., C. Linke, O. Mohler, K.-H. Naumann, H. Saathoff, R. Wagner, U. Schurath, and B. Wehner (2005), Absorption amplification of black carbon internally mixed with secondary organic aerosol, *J. Geophys. Res.*, *110*, D19204, doi:10.1029/2005JD006046.

Schulz, M., et al. (2006), Radiative forcing by aerosols as derived from the AeroCom present-day and pre-industrial simulations, *Atmos. Chem. Phys.*, *6*, 5225–5246, doi:10.5194/acp-6-5225-2006.

Schwarz, J. P., J. R. Spackman, R. S. Gao, L. A. Watts, P. Stier, M. Schulz, S. M. Davis, S. C. Wofsy, and D. W. Fahey (2010), Global-scale black carbon profiles observed in the remote atmosphere and compared to models, *Geophys. Res. Lett.*, *37*, L18812, doi:10.1029/2010GL044372.

Sokolik, I., A. Andronova, and T. C. Johnson (1993), Complex refractive index of atmospheric dust aerosols, *Atmos. Environ., Part A*, *27*, 2495–2502.

Ten Hoeve, J. E., L. A. Remer, and M. Z. Jacobson (2011), Microphysical and radiative effects of aerosols on warm clouds during the Amazon biomass burning season as observed by MODIS: Impacts of water vapor and land cover, *Atmos. Chem. Phys.*, *11*, 3021–3036, doi:10.5194/acp-11-3021-2011.

Toon, O. B., C. P. McKay, T. P. Ackerman, and K. Santhanam (1989), Rapid calculation of radiative heating rates and photodissociation rates in inhomogeneous multiple scattering atmospheres, *J. Geophys. Res.*, *94*, 16,287–16,301, doi:10.1029/JD094iD13p16287.

Torres, O., A. Tanskanen, B. Veihelman, C. Ahn, R. Braak, P. K. Bhartia, P. Veefkind, and P. Levelt (2007), Aerosols and surface UV products from OMI observations: An overview, *J. Geophys. Res.*, *112*, D24S47, doi:10.1029/2007JD008809.

Twomey, S. A. (1972), The effect of cloud scattering on the absorption of solar radiation by atmospheric dust, *J. Atmos. Sci.*, *29*, 1156–1159, doi:10.1175/1520-0469(1972)029<1156:TEOCSO>2.0.CO;2.

Warner, J. (1968), A reduction in rainfall associated with smoke from sugarcane fires—An inadvertent weather modification?, *J. Appl. Meteorol.*, *7*, 247–251, doi:10.1175/1520-0450(1968)007<0247:ARIRAW>2.0.CO;2.

Wilkerson, J. T., M. Z. Jacobson, A. Malwitz, S. Balasubramanian, R. Wayson, G. Fleming, A. D. Naiman, and S. K. Lele (2010), Analysis of emission data from global commercial aviation: 2004 and 2006, *Atmos. Chem. Phys.*, *10*, 6391–6408, doi:10.5194/acp-10-6391-2010.

Zhang, R., A. F. Khalizov, J. Pagels, D. Zhang, H. Xue, and P. H. McMurry (2008), Variability in morphology, hygroscopicity, and optical properties of soot aerosols during atmospheric processing, *Proc. Natl. Acad. Sci. U. S. A.*, *105*, 10,291–10,296, doi:10.1073/pnas.0804860105.

Zhang, X., Y.-H. Lin, J. D. Surratt, P. Zotter, A. S. H. Prevot, and R. J. Weber (2011), Light-absorbing soluble organic aerosol in Los Angeles and Atlanta: A contrast in secondary organic aerosol, *Geophys. Res. Lett.*, *38*, L21810, doi:10.1029/2011GL049385.

Zhuang, B. L., L. Liu, F. H. Shen, T. J. Wang, and Y. Han (2010), Semidirect radiative forcing of internal mixed black carbon cloud droplet and its regional climatic effect over China, *J. Geophys. Res.*, *115*, D00K19, doi:10.1029/2009JD013165.

M. Z. Jacobson, Department of Civil and Environmental Engineering, Stanford University, Yang and Yamazaki Environment and Energy Building, Rm. 397, Stanford, CA 94305-4020, USA. (jacobson@stanford.edu)